The Dissertation Committee for Kenrick John Williams Certifies that this is the approved version of the following Dissertation:

Electron Transfer in Sensitized TiO_2 Systems Studied by Time Resolved Surface Second Harmonic Generation

Committee:

Xiaoyang Zhu, Supervisor

Allen Bard

Peter Rossky

Lauren Webb

Brian Korgel

Electron Transfer in Sensitized TiO_2 Systems Studied by Time Resolved Surface Second Harmonic Generation

by

Kenrick John Williams, B.A., M.S.

Dissertation

Presented to the Faculty of the Graduate School of

The University of Texas at Austin

in Partial Fulfillment

of the Requirements

for the Degree of

Doctor of Philosophy

The University of Texas at Austin

May 2012

Acknowledgements

I would like to thank my advisor Xiaoyang Zhu for making himself constantly available for discussion, insight and guidance. He has served as an example of exemplary scientific conduct and his passion for research has been an inspiration. As a result, I have grown as a scientist.

I would also like to acknowledge all of my collaborators and the entire Zhu research group for much needed discussion, collaboration and support. Specific acknowledgement needs to be given to William Tisdale, from whom I learned about SHG, and Cory Nelson, whose help with synthesis, sample preparation and characterization made much of this work possible.

Finally, I would like to thank my wife Amanda and my family for their patients, support, love and motivation.

Electron Transfer in Sensitized TiO_2 Systems Studied by Time Resolved Surface Second Harmonic Generation

Kenrick John Williams, Ph. D.

The University of Texas at Austin, 2012

Supervisor: Xiaoyang Zhu

Obtaining abundant, clean, sustainable energy has become an increasingly large need globally. To date, solar cells have had a limited impact in meeting energy demands. This is primarily due to their relatively high cost and low power conversion efficiencies. Sensitized solar cells, or Grätzel cells, have the potential for being made with low cost materials, and achieving power conversion efficiency high enough to economically compete with fossil fuels. Understanding the dynamics of charge carriers as they separate at the interface of the light absorbing donor and their semiconducting acceptor becomes an important first step in the realization of an inexpensive and efficient sensitized solar cell.

Presented is the theory of treating electrons at donor-acceptor interfaces, and why time-resolved surface second harmonic generation (TR-SHG) is used to probe the dynamics of charge carriers at these interfaces. A series of experiments are described where various preparations of thin films of sensitizers on single crystal titanium dioxide, a common acceptor in Grätzel cells, are prepared and studied. TR-SHG studies of thin films of colloidal PbSe and CdSe QDs showed remarkably different electron cooling and transfer dynamics. The electron cooling in PbSe is thermally activated in PbSe QDs. By cooling samples, electron transfer from higher excited "hot" states was observed. Contrary, for CdSe QDs electron transfer rates were dependent on the energy of the

excited state. When higher states were excited, charge transfer rates decreased, indicating that only low energy, electrically "cold", states participate in charge transfer. When carbon based grapheme QDs are used, the electron dynamics mimic PbSe QDs. In this system, increasing the pump energy leads to slower recombination rates, indicating that electrons have to drift further back to the interface.

Table of Contents

List of Figures

Chapter 1: Introduction

Energy demands continue to increase at a rate greater than our energy production. The impact of traditional methods of energy production on the environment has become an apparent problem. The need for abundant, clean energy has become perhaps the most pressing issue facing humanity. The most abundant and fundamental energy source, which has predominantly fueled nature, is the sun. Roughly enough solar energy strikes the surface of the sun in one hour ($4.3x10^{20}\ J$) to meet annual global energy consumption ($4.3x10^{20}\ J$ in 2008) (*1*). Solar energy has the potential provide necessary, low environmental impact, energy that can be made available to areas with little or no energy infrastructure. Although we currently have the ability to capture solar energy, it is currently not considered economical to replace fossil fuels, such as coal, with solar energy. Two factors that have kept the price of solar energy high are manufacturing cost and low efficiency. Figure 1.1 illustrates this by comparing the cost and efficiency of different types of solar technologies, to be considered an economical alternative, a solar technology should cost below (above and left) of the $0.50/W line.

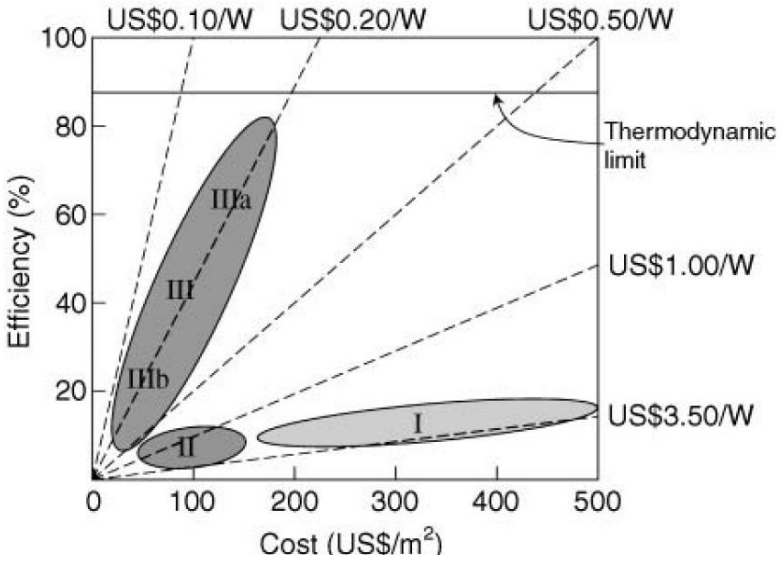

Figure 1.1: Cost-efficiency comparison of the three generations of solar cell technology: (I) silicon wafer-based, (II) thin-film, and (III) emerging technologies. Generation III technology is still in its infancy and the shaded area in this figure is meant to represent the potential of optimized devices. From (2), originally adapted from (*3*).

Solar technologies are commonly classified into three generations based on what kind of platform they are based (*4*). The "first generation" is based on silicon wafers. This type of solar cell is characterized by high manufacturing cost, but near theoretically limited efficiency. The "second generation" technologies are based on thin film solar cells based on low cost deposition of various semiconducting materials, but the cost savings are almost entirely offset by reduced performance. Generation III or "emerging" solar technologies are anticipated based on designs that do not suffer from the same efficiency limits as traditional solar cells, but are still being developed, and have yet to be realized.

1.1.2 How Efficient can a Solar Cell Be?

The second law of thermodynamics puts a fundamental limit of the efficiency of converting energy to work. This fundamental limit, described by the Carnot theorem, where $\eta = 1 - T_C/T_H$, states the upper bound for a heat flow from a hot source exhausting to a cold environment. When we consider the sun $T_H = 6000K$ and earth $T_C = 300K$ as our source and sink, we arrive at a Carnot efficiency of $\eta = 95\%$. This limiting case would involve the generation of no entropy. Planck showed that the emission and absorption of radiation involves an unavoidable production of entropy (*5*). Consequently a more accurate description for the absolute efficiency of solar energy conversion is to consider the sun and earth as two bodies re-emitting radiation reciprocally. The corresponding *black body limit* for the sun and earth is $\eta = 86.8\%$ (*4*). Because this limit requires the flow of energy to be entirely contained within the solid angle of the terrestrial solar cell subtended by the sun, which when you consider the absorption of our own atmosphere, makes this direct efficiency unrealistic. It is more relevant to compare most solar cell designs by the diffuse efficiency limit ($\eta = 68.2\%$) which reflects loss of energy by radiative heat transfer to the environment (*4*).

Although this limit should seem much more attainable than the direct efficiency, typical commercial p-n junction solar cells have efficiencies of only ~15%. The major loss of efficiency in the p-n junction solar cell is thermalization of electrons absorbed above the semiconductor band gap. Shockley & Queisser showed that the maximum efficiency a standard single-junction solar cell can achieve is 31.0%, at an optimal band gap of 1.3 eV (*6*). This limit arises from the fact that any photon with $E > 1.3\,eV$ can only contribute a maximum of 1.3 eV, and any photon with $E < 1.3\,eV$ does not contribute at all.

The theoretical efficiency of the p-n junction is quickly improved if you are allowed to add additional stacked junctions. A stack of just two ideal p-n junctions has a maximum efficiency of 42.9% (1.87eV and 0.98eV), and an infinite stack of ideal p-n junctions reaches the diffuse efficiency limit of 68.2%. The problem with this design is that although they boast the best efficiency (42% for a three-cell stack), multistack p-n junction solar cells are complicated and expensive to build.

1.1.2 What are Emerging Solar Technologies?

The limited design flexibility of the p-n junction solar cell has implies that the future of solar cells lies in an entirely different direction. In 1991, Grätzel and co-workers introduced a radically different solar cell based on a wide band gap semiconductor sensitized with a metal-organic dye and a redox couple (*7*). This "dye-sensitized solar cell (DSSC)" works by covering a mesoporous matrix of a wide band gap semiconductor (sintered TiO_2), deposited on a transparent electrode (anode) with a metal-organic ruthenium dye, immersed in an electrolyte solution (I^-/I_3^-), to form a high surface area contact between the cathode and dye covered semiconductor (Figure 1.2). Many of the components of the cell can be synthesized in solution, eliminating much of the high manufacturing cost associated with p-n junction cells. DSSC are capable of efficiencies of ~10%.

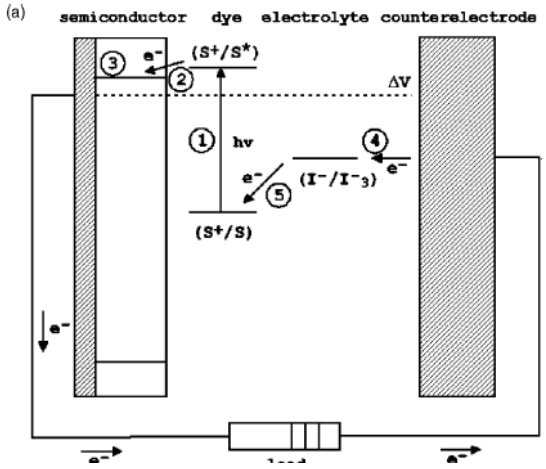

Figure 1.2: Dye Sensitized Solar Cell from (*7*).

Since the advent of the dye cell, numerous similarly configured "excitonic" solar cells have been designed (*8*). Many of these new devices are based on a light absorber in high-surface-area contact with separate electron-transporting and hole-transporting phases. The light absorber need not be distinct from either of the transporting phases, but all of these cells rely on high surface area interfaces for charge separation. Examples of such devices include: i) quantum dot-sensitized solar cells (*9,10*), where the dye is replaced by semiconductor nanocrystals, or "quantum dots", ii) all-quantum dot heterojunction solar cells, based on a high surface area interface between two quantum dot layers (*11,12*) iii) organic bulk heterojunction solar cells (*13-15*) consisting of two or more blended semiconducting polymer/organic phases, and iv) hybrid organic-inorganic heterojunction solar cells (*16,17*) combining a polymer/organic phase and a nanostructured inorganic phase.

It has been noted that the physical mechanism responsible these excitonic solar cells is fundamentally different from that of the p-n junction (*8*). In p-n junction solar cells, absorption of sunlight results directly in free electrons and holes which are readily separated by the built-in field of the p-n junction. In excitonic solar cells, there is no

built-in field. Further, the electron and hole generated by photon absorption are localized to the same molecule or quantum dot. The most important step in the generation of photocurrent is separation of these electron-hole pairs at an interface where there is favorable alignment of energetic levels. Knowledge of the fundamental mechanisms underlying interfacial charge separation is paramount in understanding and improving excitonic solar cells.

1.1.3 Quantum Dot Solar Cells

Semiconducting nanocrystals or quantum dots (QDs) are attractive materials for next generation photovoltaic devices. When the size of a semiconducting material is reduced below the natural length scale of the electrons within the material, its properties are changed by this confinement. Most notably its optical absorption spectrum changes from the single step like band edge characteristic of bulk semiconductors to a series of discrete atomic like transitions. This is illustrated in Figure 1.3. As Dimensionality is reduced, the density of states of a semiconductor becomes more discrete.

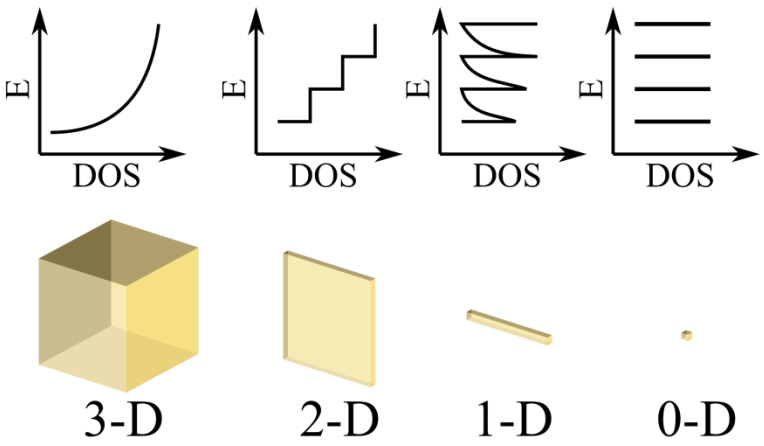

Figure 1.3: Effects of confinement in different dimensions on the density of states.

The ability to use one material with a variety of different band gaps and optical transitions has great implications for photovoltaics. Because QDs can be synthesized as a solution processable colloidal dispersion, quantum dot solar cells can be fabricated by large-area low-temperature manufacturing techniques such as roll-to-roll transfer, dip coating, spin casting, or inkjet printing, which can offer significant cost savings compared to high-temperature vacuum techniques and enable integration with flexible substrates.

Beyond size dependant optical absorption, quantum dots have novel size dependant properties that could lead to high efficiency solar cells. One of these processes is the efficient conversion of a single high energy photon to multiple lower energy carriers (*18,19*). By converting one photon of $hv > 3E_g$, to three electron-hole pairs, some or all of the losses to carrier thermalization could be avoided. This process, named carrier multiplication (*18*) or multiple exciton generation (*19*) has become a source of some skepticism after the consensus became that some of the initial claims were overstated due to varying sample conditions (*20,21*). However, other quantum confinement properties may lead to breakthroughs in solar efficiency.

Another exciting property of quantum confined systems is that they exhibit long hot carrier lifetimes due to slowed thermalization of photogenerated carriers. By collecting charge carriers before they have had time to give energy to the nuclear coordinate (phonons), it should be possible to increase the efficiency of solar cells. In fact, if a zero bandgap semiconductor with no electron phonon scattering existed, it would be possible to make a solar cell with a diffuse efficiency of ~66% (*22*). In order to capture all of the energy from ”hot” carriers, as electrons and holes are removed from a material, electron-electron scattering events would need to re-equilibrate the energy distribution of charge carriers, such that some of the energy from the highest energy

charge carriers be given to low energy charge carriers. An illustration of what such a hot carrier solar cell may look like is shown in Figure 1.4.

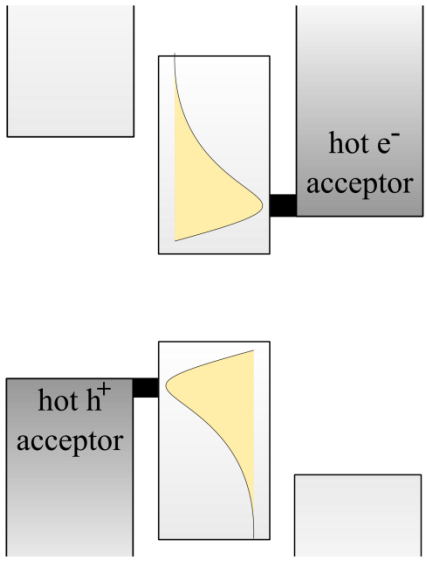

Figure 1.4: Illustration of possible "Hot Carrier Solar Cell", where unthermalized carriers are left scatter with one another, while transfer only occurs at a specific energy for electrons and holes, and hot carriers equilibrate into Boltzmann's distributions.

An ideal material for a hot electron solar cell would have very low electron-phonon scattering rates, high electron-electron scattering rates and a very small bandgap. Fortunately there is a material which posses these unique qualities, graphene. Recently, a synthetic route for large solution stable graphene QD has been demonstrated (*23*).

1.1 MOTIVATION AND ORGANIZATION OF THESIS

Although quantum dots have played host to a variety of solar cell designs, there are still many outstanding fundamental questions about the nature of charge separation at interfaces with these materials. These questions include: What are the mechanisms of charge transfer from "hot" and thermally relaxed states? What role does delocalization

and electron coupling play in the energy of excitonic transitions and how does that affect charge transfer? What are possible pathways for charge transfer? What barriers limit charge transfer/separation?

The motivation of this thesis is to experimentally investigate and answer some of these questions. Chapter 2 presents a brief theoretically framework from which these problems can be approached. Detailing the physical properties of quantum confined materials, as well as reviewing other work that has contributed to the current understanding of quantum dot to semiconductor charge transfer, specifically at sub-nanosecond time scales. Chapter 3 describes the how an ultrafast spectroscopy technique, time resolved second harmonic generation, can be used to probe ultrafast transient fields at interfaces. In Chapter 4, we investigate how making 3-Dimensional and 2-Dimensional assemblies of our model system (PbSe QDs on single crystal TiO_2) affect their optical and electrical properties through changes in their surface chemistry, the local electronic coupling and dielectric of the surrounding matrix. Chapter 5 details the investigation into the role of delocalization of excitons into determining the pathway for electron transfer. Finally, Chapter 6, a summary of investigations into how hot electron transfer, reported for the first time from PbSe QDs to TiO_2 (*24*), can also be observed in the ideal hot electron solar cell material, graphene QDs.

Chapter 2: Background and Theory of Zero-Dimensional Quantum Confined Systems

In this chapter we discuss how quantum confinement can lead to unique physical properties that have applications in solar cell design. From there, two different types of zero-dimensional quantum confined materials are introduced, Semiconducting nanocrystals and graphene quantum dots. A theoretical framework is developed for the treatment of charge transfer from quantum dots to semiconductor acceptors.

2.1 QUANTUM CONFINEMENT

Quantum size effects occur when the size of the material is less than the natural length scale of the electron and hole. A good approximation of the natural length scale of a charge carrier is the Bohr radius. In general, the Bohr radius of a particle is defined as

$$a_B = \varepsilon \frac{m}{m^*} a_0 \qquad (2.1)$$

where ε is the dielectric constant, m^* is the mass of the particle, m is the rest mass of the electron and a_0 is the Bohr radius of the hydrogen atom (*25*). Three different Bohr radii are important when describing a quantum dot, the Bohr radii of: the electon a_e, the hole a_h and the exciton a_{exe}. With these values, three limits can be considered (*26)*. For a quantum dot of radius a, one limit is when $a < a_e < a_h < a_{exe}$, the electron, hole and exciton are all strongly confined by the core, this is known as the *strong confinement regime*. Another is when $a_e < a_h < a < a_{exe}$, where only the center-of-mass motion of the exciton is confined. This is known as the *weak confinement regime*. Finally, when a is between the charge carriers, (i.e. $a_e < a < a_h < a_{exe}$). This is known as the *intermediate confinement regime*.

It is useful to describe a quantum dot by the confinement regimes, but for a quantitave description of the size dependent electronic properties of these materials is it useful to describe them with a simple *particle-in-a-sphere* model (*27*).

For the case of a nanocrystal, if a is significantly larger than the lattice constant, you can express the quantum dot as a linear combination of Bloch functions (*29*),

$$\Psi_{sp}(\vec{r}) = \sum_{\mathrm{k}} C_{nk}\, u_{nk}(\vec{r}) \exp(i\vec{k}\cdot\vec{r}), \qquad (2.2)$$

where the functions u_{nk} have the periodicity of the crystal lattice. Since u_{nk} generally have a weak *k*-dependence, then Eq. (2.2) can be written as

$$\Psi_{sp}(\vec{r}) = u_{n0}(\vec{r}) f_{sp}(\vec{r}), \qquad (2.3)$$

where the functions $f_{sp}(\vec{r})$, are the single particle envelope functions,

$$f_{sp}(\vec{r}) = \sum_{\mathrm{k}} \mathrm{C}_{\mathrm{Nk}} \exp(i\vec{k}\cdot\vec{r}). \qquad (2.4)$$

In general, this model considers an arbitrary particle of mass m_0 inside a spherical potential well or radius *a,* with square walls,

$$V(r) = \begin{cases} 0, & r < 0 \\ \infty, & r > 0 \end{cases}. \qquad (2.5)$$

Following Zettili (*28*), the solution to the Schrödinger equation is

$$f_{sp}(\vec{r}) = \Phi_{n,l,m}(r,\theta,\phi) = C\, \frac{j_l(k_{n,l}r) Y_l^m(\theta,\phi)}{r}, \qquad (2.6)$$

and eigenvalues,

$$E_{n.l} = \frac{\hbar^2 k_{n,l}^2}{2m} = \frac{\hbar^2 \alpha_{n,l}^2}{2m a^2}, \qquad (2.7)$$

where C is a normalization constant, $\alpha_{n,l}^2$ is the *n*th zero of $j_l(k_{n.l}r)$ Bessel function and $Y_l^m(\theta, \phi)$ is a spherical harmonic. Therefore, the single particle states can be described by atomic like orbitals with quantum numbers n(1,2,3…), ℓ(s,p,d…), and m. If we invoke the effective mass approximation, the particle masses in Eq. (2.7) are the effective mass of the electron or hole.

So far we have completely ignored coulombic attraction between the electron and hole. How the coulombic interaction is included depends on the confinement regime (*26*). In the strong confinement regime, the strong confinement approximation can be made, and a first order perturbation term can be added to correct for the coulombic attraction. The electron hole pair (*ehp*) states in the nanocrystal are then written (*29*),

$$\begin{aligned} \Psi_{\text{ehp}}(\overrightarrow{r_e}, \overrightarrow{r_h}) &= \Psi_{\text{e}}(\overrightarrow{r_e})\Psi_{\text{h}}(\overrightarrow{r_h}) \\ &= u_e f_e(\overrightarrow{r_e}) u_v f_h(\overrightarrow{r_h}) \\ &= C\left(u_c j_{L_e}\left(k_{n_e,L_e} r_e\right) Y_{L_e}^{m_e}\right)\left(u_c j_{L_h}\left(k_{n_h,L_h} r_h\right) Y_{L_h}^{m_h}\right) \end{aligned} \qquad (2.8)$$

The energy of the *ehp* state is then,

$$E_{ehp}(n_h L_h n_e L_e) = E_g + \frac{\hbar^2}{2a^2}\left[\frac{\alpha_{n_h,L_h}^2}{m_{eff}^v} + \frac{\alpha_{n_e,L_e}^2}{m_{eff}^v}\right] - E_c. \qquad (2.9)$$

This is known as the effective mass model.

2.1.1 Semiconducting Nanocrystals

Semiconducting Nanocrystals are a quantum confined material made from synthesizing semiconductor crystals that are smaller than the Bohr radius of their charge carriers. Solution synthesis of colloidal nanocrystals, through a hot injection of precursors (30), has led to intense exploration into the properties and potential applications of these materials. Shown in Figure 2.1a, is the growth scheme of the hot injection technique. At the time of injection (Fig. 2.1b), the concentration and temperature of the reaction are above the nucleation threshold. The injection causes a drop in temperature, combined with the effects of nucleation, reduce the concentration of precursors below the nucleation threshold. From there, growth of nanocrystals, from the precursors, continues until the precursor concentration is too low to support growth. From there, Ostwald ripening may occur, growing the larger, more stable, nanocrystals at the expense of the smaller ones. Ostwald ripening causes a broadening of the size distribution of the particles, so unless a very large size is desired, reactions are generally quench prior to this growth process.

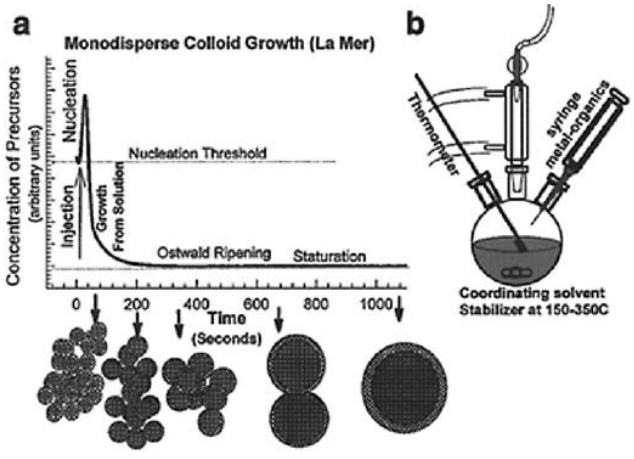

Figure 2.1: (a) Schematic of the stages of nanocrystal growth following hot injection. (b) Representation of the experimental apparatus used during synthesis. From (*31*).

In Figure 2.2A you see the effect of quantum confinement on the band structure of a semiconductor. As the quantum confinement increases, you get a larger effective bandgap and more discrete states nearing the band edge. In Figure 2.2B this can be seen for CdSe. Notice that nanocrystal sizes larger than the Bohr radius (6 nm) lack clear excitonic features.

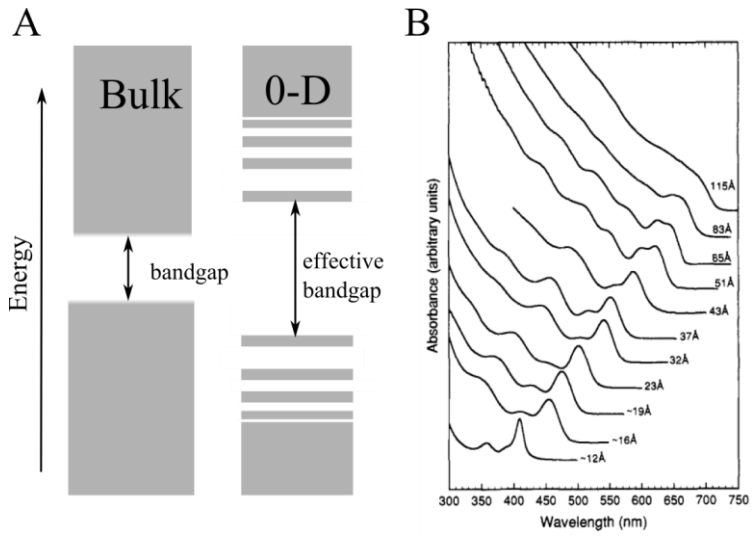

Figure 2.2: (A) Effects of quantum confinement on the density of states of semiconductors, resulting in discretized states and widening of the bandgap. (B) size dependence of the absorption spectra of CdSe nanocrystals ranging in size from 12-115Å, from (*30*)

Because of the high dielectric of semiconductors, the effects of the discontinuity of the dielectric function at the nanocrystal boundary are increased. A charged particle in a finite sized crystal will polarize its surroundings. Because more than one charged particle may be confined to a nanocrystal, the interaction with the image charges of those species needs to be considered. These classical contributions can lead to measurable solvatochromic effects on the electron-hole pair state optical transition frequency (the

peak position of the exciton absorption) (32) The overall contributions to the first exciton energy can be writing as

$$E_{EX}^{1} = E_{g}^{0} + E_{e}^{kin} + E_{h}^{kin} + E_{Coul}^{dir} + \Sigma_{e}^{Pol} + \Sigma_{h}^{Pol} + j_{e,h}^{Pol}, \qquad (2.10)$$

where E_g^0 is the bulk transport gap, E_e^{kin} (E_h^{kin}) is the kinetic energy of the electron in the conduction band (hole in the conduction band), Σ_e^{Pol} (Σ_h^{Pol}) is the polarization stabilization energy, that is the attraction an electron (hole) has to its image charge in the surrounding dielectric medium and $j_{e,h}^{Pol}$ is the polarization destabilization energy, that is the repulsion the electron (hole) feels to the image charge of its opposite charge carrier.

The total polarization correction (last three terms of Eq. 2.10) for the first exciton is given by (*32*),

$$\delta = \frac{\pi q^2}{2\varepsilon_1 \varepsilon_0 a} \sum_{l=1}^{\infty} a^{2l+1} A_l \int_0^1 [j_0(\pi x)]^2 x^{2l+2} dx, \qquad (2.11)$$

where j_0 is a spherical Bessel function, ε_1 is the dielectric of the QD core, q is the fundamental charge of the electron and a is the radius of the QD. For a quantum dot with a ligand shell, surrounded by a dielectric matrix (Figure 2.3), A_l is

$$A_l = \frac{l+1}{a^{2l+1}} \frac{a^{2l+1}(\varepsilon_2-\varepsilon_3)[\varepsilon_1+l(\varepsilon_1+\varepsilon_2)]+b^{2l+1}(\varepsilon_1-\varepsilon_2)[\varepsilon_3+l(\varepsilon_2+\varepsilon_3)]}{a^{2l+1}(\varepsilon_1-\varepsilon_2)(\varepsilon_2-\varepsilon_3)l(l+1)+b^{2l+1}[\varepsilon_1+l(\varepsilon_1+\varepsilon_2)][\varepsilon_3+l(\varepsilon_2+\varepsilon_3)]}, \qquad (2.12)$$

where ε_2 is the dielectric constant of the shell and $\varepsilon_3$is the dielectric constant of the surrounding matrix and b is the radius from the center of the core to the edge of the ligand shell.

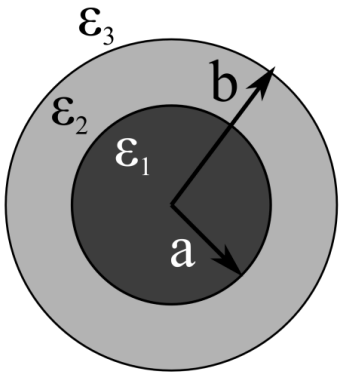

Figure 2.3: Illustration of the core/shell/matrix model for solvatochromism.

2.1.2 Graphene Quantum Dots

Graphene, consisting on a single atomic layer of graphite (Fig. 2.4), has generated considerable excitement for its unique physical and material properties. 2-Dimensional bulk graphene has a 0 eV bandgap and high extinction coefficient ($1x10^5$ M^{-1} cm^{-1}), allowing an atomic layer sheet to absorb 2.3% of incident light (*20*). Additionally the linear dispersion relationship near the Fermi level allows for conservation of energy during electron-electron scattering without requiring electron-phonon scattering. This behavior is ideal for a hot carrier solar cell material (*22*).

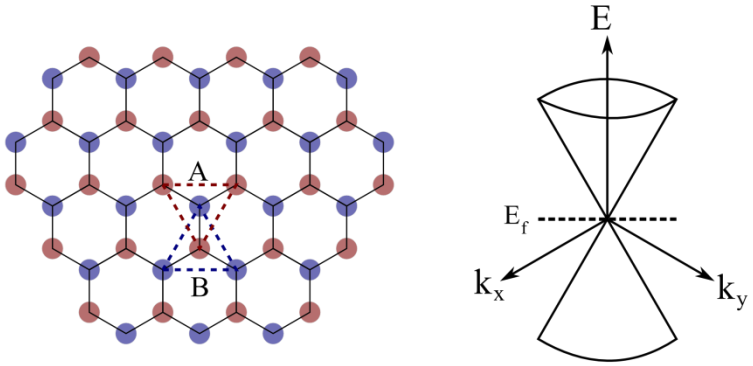

Figure 2.4: (Left) Lattice structure of graphene, consisting of two interpenetrating triangular lattices. (Right) electronic dispersion near the dirac points (located at K and K' in the brillion zone) note the linear dispersion relationship.

By controlling the size of the graphene sheet, electronic and optical properties, such as the bandgap, can be tuned. One major challenge when working with graphenes nanoparticles is their poor solubility and propensity for sticking together (forming graphitic structures). Recently, the synthesis of large, solution processable, graphenes with solubilizing side alkyl groups has been developed, leading to the realization of colloidal graphene quantum dots (QDs) (*23*). Some of the possible graphene QDs that have been synthesized are shown in Figure 2.5a.

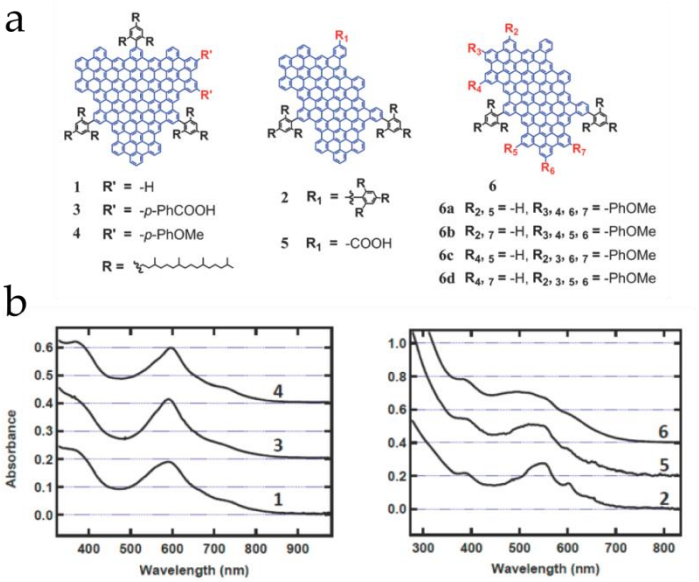

Figure 2.5: (a) Molecular structures of grapheme quantum dots. (b) UV-vis spectra of graphene QDs 1-6 in toluene. 1, 3, and 4 have equal absorption edges at ~900 nm, and 2, 5, 6 have equal absorption edges at ~760 nm. From (*23*)

By controlling the size of the conjugated carbon "core" the optical absorption energy. Fine changes to the absorption spectra and redox potential can be made through functionalization of the edge groups (*23*).

Colloidal graphene QDs have material properties that make them excellent light absorbers in photovoltaic devices (*23,33*). For example, graphene QDs have continuous absorption spectra in the UV-visible region due to the overlap of electronic absorption bands caused by closely spaced electronic energy levels and vibronic coupling (*23,*34) A bulk sheet of graphene has a 0 eV bandgap and incredibly high extinction coefficient, allowing an atomic layer sheet to absorb 2.3% of incident light **(***35***).**

Graphene QDs have also been shown to have slow hot-carrier cooling dynamics (36) reminiscent of the "phonon bottleneck" which has been intensively investigated in conventional semiconductor quantum dots (*37).*

2.2 THERMALIZATION OF HOT CARRIERS IN QUANTUM CONFINED STRUCTURES

Because the discrete states in quantum confined materials may be separated by large energies relative to the LO phonon frequencies, phonon-assisted relaxation between these discrete electronic states may require emission of multiple phonons. Since the phonon-assisted relaxation is the primary mechanism for carrier cooling in bulk semiconductors, it was theorized that carrier cooling in quantum dots should be slower than in bulk semiconductors because of the low probability of multiphonon processes (i.e., "phononbottleneck") (*38*). In reality, quantum dots may relax by alternative relaxation mechanisms efficient enough to result in subpicosecond carrier cooling that is not significantly slower than that in bulk materials (*37,39*). Auger processes allow hot electrons to relax rapidly by transferring energy to holes, which often have a greater effective mass and thus smaller energy spacing, making it easier for the holes to relax through phonon-assisted pathways (Figure 2.5) (*40,41*), or non-adiabatic channels involving surface ligands (*42,*43), Trap states (*44,*45) in the quantum dots and high frequency vibrational modes in surface ligands (*46*).

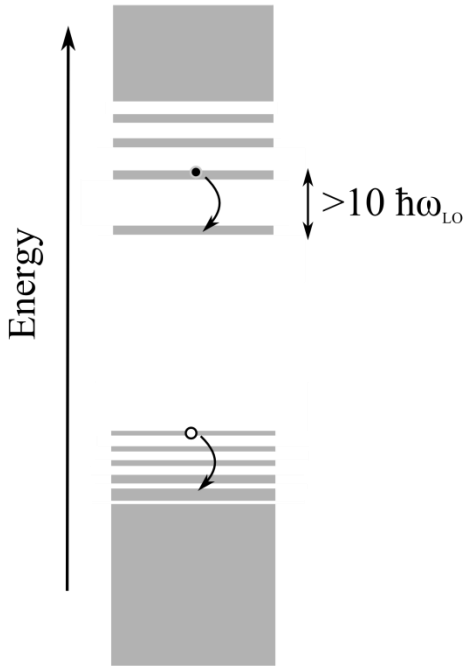

Figure 2.5: Illustration of a quantum confined material with discrete states separated by more than 10 times the energy of an LO phonon and a heavier effective mass hole. Note the hot electron relaxation through an Auger process, giving its energy to the hole, which has smaller energy spacing due to higher effective mass.

2.3 ELECTRON TRANSFER IN QUANTUM DOTS

This section reviews some basics of quantum mechanical tunneling and considers how the presence of bridge molecule can influence the tunneling transmission probability. Next, we discuss the Marcus theory for non-adiabatic electron transfer, wherein we consider the effects of nuclear coordinates and the thermal bath on electron transfer in condensed phases and at surfaces. The role of interfacial electronic coupling and how this important parameter can strongly influence the way we think of electron transfer is discussed.

2.3.1 Tunneling

Electron transfer between a QD linked to a semiconductor can be first described as a bridge-mediated process, where electrons tunnel from one material to the next across the bridge (ligand or functional group attaching QD to semiconductor acceptor). Tunneling can most simply be described as a particle with energy E incident on a barrier of height $V(x) > E$, as shown in Figure 2.6. A classical particle would not be able to penetrate this barrier, but a quantum mechanical particle has some probability of doing so. This transmission probability is equal to the ratio of the square of the amplitudes of the transmitted and incident wave functions. A method for estimating transmission probability of the incident particle can be made using the Wentzel-Kramers-Brillouin (WKB) approximation, where we assign wave vectors of the form (*28*)

$$k(x) = \begin{cases} \hbar^{-1}\sqrt{2m[(E - V(x)]} & E \geq 0 \\ i\hbar^{-1}\hbar^{-1}\sqrt{2m[(V(x) - E]} & x \leq 0 \end{cases}, \qquad (2.13)$$

where *m* is the mass of the particle. The transmission coefficient is given by,

$$T \sim exp\left[-\frac{2}{\hbar^{-1}} \int_{X_1}^{X_2} \sqrt{2m[(V(x) - E]}\, dx\right]. \qquad (2.14)$$

Although the WKB approximation is only quantitative for smoothly varying potentials, it is still qualitatively valid in describing the dependence on distance and height regardless. Equation (2.14) tells us that the transmission probability decreases exponentially with barrier width and by the square root with respect to barrier height.

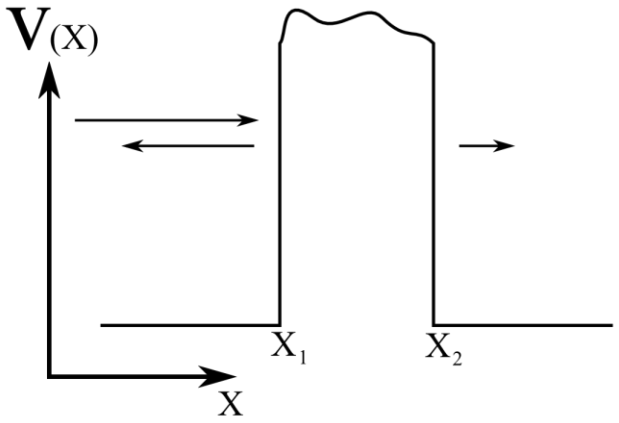

Figure 2.6: Tunneling of a quantum mechanical particle through a barrier of arbitrary shape. Some fraction of the wave is transmitted while the rest is reflected back.

In the example of bridge mediated electron transfer, the bridge acts as a tunneling barrier to electron transfer. However, unoccupied states (i.e. LUMO) in the bridge may act to raise or lower the potential height of the bridge. This mechanism of bridge energy level-mediated charge transfer is known as *superexchange*. Although the electron may never reside in the molecular orbital, its presence can serve to facilitate charge transfer. Superexchange rates are often epressed in terms of a "β" value for the bridge (*47*),

$$k_{ET} = k_{tunn} = k_0 \exp(-\beta d_{DA}), \qquad (2.15)$$

where d_{DA} is the distance between donor and acceptor (bridge length). This expression shares the same dependence on barrier width as derived from the WKB approximation in Eq. (2.14). The energy dependence is contained in the β value. These values can be determined from experimentally determined tunneling rates based on the number of

repeating units in a molecular bridge. Typical β values are 0.2-0.6 $Å^{-1}$ for highly conjugated chains, 0.9-1.2 $Å^{-1}$ for a saturated hydrocarbon and ~2 $Å^{-1}$ for vacuum (*47*)

2.3.2 Non-adiabatic Electron Transfer

The theory of non-adiabatic electron transfer presented in this chapter is often referred to as "Marcus theory" or a "Marcus picture" of electron transfer, named for Rudolf Marcus, who won the Nobel Prize in Chemistry in 1992 for his pioneering work in the field.

If we consider two states, a donor (D) and an acceptor (A), in a polar solvent, we know that the solvent will have reorganized to stabilize the electron on the donor state. If that electron where to transition to the acceptor state on a timescale much faster than the motion of the solvent, the solvent would no longer be in a stable configuration, and would reorganize, releasing free energy until the most stable configuration is reached. This *reorganization energy* (λ) typically has values of ~0.1-1 eV for aqueous solutions (48). Marcus observed that if the electron transfer step were to proceed simply as described, it would generate λ with excess energy–considerably more than the available k_BT at room temp (49). Electron transfer in aqueous solutions is observed to occur at reasonable rates, indicating the mechanism must be different. Marcus reasoned that, because of the disparity in times scales between electron transfer and nuclear motion, electron transfer will occur only if the donor and acceptor an in a configuration such that the charge transfer step is energy conserving. This meaning that the nuclear configuration at the instance of charge transfer is one in which the free energy of the system does not change whether the electron is found on the donor or the acceptor. The activation energy for such charge transfer is only the energy required to deform the nuclear coordinates to the charge transfer configuration. This is illustrated in Figure 2.7.

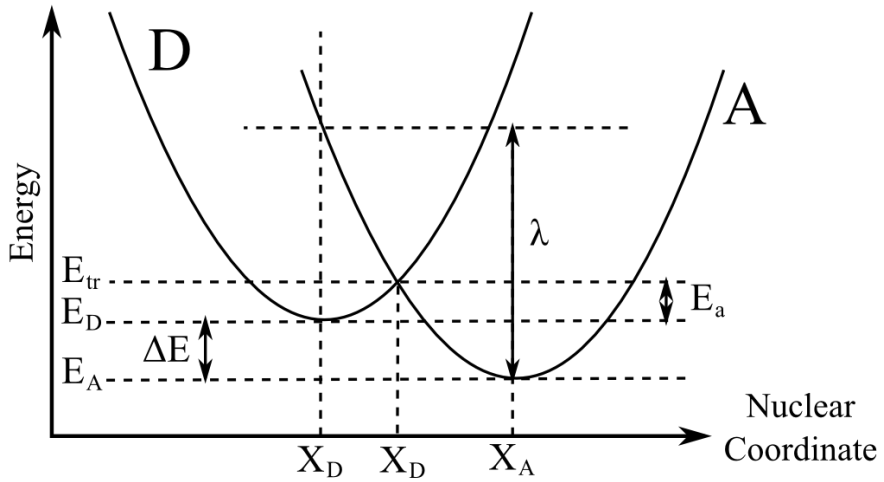

Figure 2.7: Diabatic free energy surfaces for two system states D and A corresponding to localization of an electron on a donor or acceptor species, respectively. The X-coordinate represents nuclear configuration of the system. When $X=X_D$, the nuclear environment has arranged itself in such a way as to stabilize the electron on the donor species. Similarly, when $X=X_A$, the electron is stabilized on the acceptor species.

2.3.2 Adiabicity and Electronic Coupling

Marcus theory has found broad application in many systems; it is not valid for all systems, including QDs on the surface of a bulk semiconductor acceptor. The Marcus theory assumes that thermally activated rearrangement of nuclear coordinates is the rate limiting step in electron transfer. Further it assumes that electronic coupling is weak enough that it can be treated perturbatively via Fermi's golden rule. This is not the case, especially when electronic coupling is strong relative to the reorganization energy, electron transfer proceeds adiabatically. Instead of thinking of charge transfer as a discrete event between two localized states, it is useful to think of the charge transfer reaction as a time dependent rearrangement of charge along a continuous equilibrated potential energy surface (Fig 2.8).

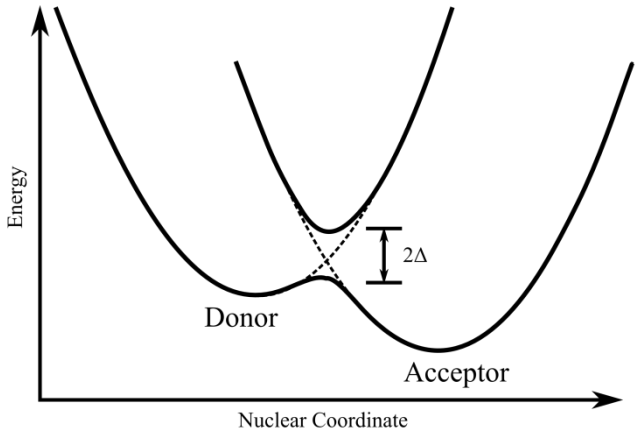

Figure 2.8: Nuclear potential energy surfaces for an electron donor-acceptor system. The x-axis represents various states of molecular organization, and the reorganization energy λ is the amount of energy that would be released if electron transfer were to proceed vertically (i.e. with nuclear coordinates frozen). The dotted (crossing) curves are parabolic diabatic free energy surfaces for separate donor and acceptor species in the weak-coupling limit, wherein the thermal activation energy for electron transfer is completely determined by nuclear rearrangement. The solid (anti-crossing) curves are adiabatic free energy surfaces of the coupled donor-acceptor system.

at surfaces, the donor-acceptor interaction can be understood as a adsorbate-subrate interaction and may be handled within the framework of chemisorptions theories, which deal with the coupling of atomic or molecular orbitals to electronic bands in solids. When considering the case of a single valence state $|m\rangle$ with a substrate band $|k\rangle$; if the adsorbate level is located in the large substrate band, the projection of the density of eigenstates of the total Hamiltonian onto the adsorbate is (*50*),

$$N_m(E) = \frac{1}{\pi}\frac{\Delta(E)}{(E-E_m)^2+\Delta(E)^2}, \qquad (2.16)$$

where E_m is the original energy of the valence orbital and $\Delta(E)$ is given by,

$$\Delta(E) = \pi \sum_k |V_{mk}|^2 \delta(E - E_k), \qquad (2.17)$$

Equations (2.16) and (2.17) show how the interaction of the valence state with the substrate band form an adsorbate resonance with a broadened Lorentzian line shape by width 2Δ.

The term Δ as defined in Equation (2.17) is a measure of the electronic coupling strength between an adsorbate, such as a quantum dot and a substrate electronic band, such as the conduction band of TiO_2. Surface electron transfer processes are generally discussed within three coupling regimes, depending on the relative magnitude of Δ and λ. The first regime, $\Delta \ll 2\lambda/\pi$, is where Δ has little effect on the activation energy for charge transfer, which is determined almost entirely by λ. This is the Marcus limit, as described in section 2.3.1. The second regime, $k_B\mathrm{T} < \Delta \leq 2\lambda/\pi$, is the intermediate coupling regime. In this regime, electron transfer is still a thermally activated process and dependant on nuclear rearrangement, but the constraints on the charge transfer nuclear configuration are lifted to some extent. Third and finally, $\Delta > 2\lambda/\pi$, we have reached the strong coupling regime, where nuclear rearrangement plays little to no role in charge transfer. In the strong coupling regime, donor and acceptor states are no longer distinguishable, and the donor state is itself an eigenstate of the entire coupled system. Charge transfer in this regime occurs on the femtosecond or sub-femtosecond time scales.

Estimates of the interfacial coupling energy Δ can be obtained from measurements of nearest-neighbor coupling between nanocrystals. The nearest neighbor coupling of PbSe QDs has been measured by Liljeroth and coworkers to be as large as 25 meV) (*51*). It is reasonable to estimate that the coupling to the substrate might be half of that coupling between QDs, such that $V_{mk} \approx 12\, meV$. Using Equation (2.17) we obtain an interfacial coupling energy $\Delta \approx \pi |V_{mk}|^2 \approx 450\, meV$. This is much larger than the

reorganization energy predicted from this system, $\lambda = 15 - 25\ meV$ (see chapter 4 for more details), placing the system in the strong coupling regime where, $\Delta > 2\lambda/\pi$. In this coupling regime, the electron transfer time constant, or more accurately speaking, the redistribution time, can be approximated by (*52*),

$$\tau \sim \hbar/\Delta. \qquad (2.18)$$

For $\Delta \approx 450\ meV$ the redistribution time is only a few femtoseconds. This theoretical approximation agrees with results from our lab, where electron transfer to photoexcited PbSe QD happens below the time resolution of the experiment (<30 fs), this is discussed further in chapters 5 and 6.

2.4 PREVIOUS EXPERIMENTAL INVESTIGATIONS

To experimentally resolve the dynamics of electron transfer events, ultrafast spectroscopic techniques, involving sub-picosecond pulsed lasers are often necessary. Ultrafast time-resolved spectroscopy is often referred to as *pump-probe* spectroscopies due to the use of two laser pulses, the first (*pump* pulse) is used to excite the system, the second (*probe* pulse) is used to monitor how the system has changed after some delay in time. In such experiments, femtosecond time resolution is achieved by varying the relative spatial delay the pump and probe pulses must travel before reaching the sample. Experimental observables probed by the second probe commonly include fluorescence, absorption, photoemission, changes in the linear (e.g. reflectivity, transmittivity) and non-linear (e.g. sum- and difference-frequency generation) optical response of the system.

One technique which has been proven useful for studying femtosecond electron dynamics is transient absorption (TA) spectroscopy. In TA experiments, a pump pulse is

used to photoexcite the sample, and then a probe pulse measures changes in the absorption spectra, commonly bleaching due to increased population of the excited state. TA has commonly been used to investigate charge transfer from dye molecules to wide band semiconductors, most notably TiO_2 (*53,*54). In these studies, the intra-band transitions in the semiconductor are probed using a mid-IR probe wavelength, to detect the presence of electrons that have transferred to the acceptor. The vibrational spectrum of the dye is also probed to, measuring changes that are sensitive to the oxidation state of the dye. Because many photons need to be absorbed, it is difficult to study interfacial charge transfer. To generate reasonable signal-to-noise ratios, high surface area samples are required, limiting the ability to study controlled interfaces consisting of a sub-monolayer adsorbed directly to a well defined crystal surface.

Charge separation has been widely investigated for quantum dot/wide band gap semiconductor systems, including CdS, PbS, Bi_2S_3, CdSe, InP and InAs to TiO_2 or SnO_3 (see (*55*) or (*56*), and the references cited therein), but have generally employed steady state techniques (such as fluorescence quenching) or electrical measurements from model devices (such as solar cells) to demonstrate interfacial charge separation. Most notable, recent attempts have looked at more ordered polycrystalline samples, offering insight into the importance of surface states as channels for electron transfer in CdSe/TiO_2 electron transfer (57). The authors note that charge transfer rates seem to increase in polycrystalline systems with higher concentration of surface defects. A growing number of papers have addressed the kinetics of interfacial electron transfer from QDs to wide band gap semicondor acceptor (*10*,*58*-61), however, the results have been mixed, reporting rates that vary over orders of magnitude.

The difficulty in using TA to probe quantum dot-to-semiconductor charge transfer is the convolution of dynamic contributions from electron transfer, intraband absorption,

electron trapping, hole quenching, and hot carrier relaxation. The mid IR absorption that has worked so well for dye-to-semiconductor studies is no longer reliable as the quantum dots often have transitions (such as a $1S_e \rightarrow 1P_e$) and therefore probe both the transferred and un-transferred electrons. In an attempt to avoid these problems, TA studies have tried to use the recovery after photo bleaching of the first exciton transition ($1S_h \rightarrow 1S_e$) with the nanocrystal, characteristic of the electron population of the $1S_e$ state. Occupation of the state reduces the transition probability between these states. Recovery of this bleach is would be typical of charge transfer, where the $1S_e$ is no longer occupied and therefore no longer bleached, however, the removal of electrons from the $1S_e$ can be attributed to multiple processes, including: electron transfer, recombination, surface trapping and Auger processes involving $1S_e$ electrons. To account for many of these other mechanisms of bleach recovery, the dynamics of the donor/acceptor system are compared to the dynamics of a system of isolated QDs. The electron transfer rate is then determined by,

$$k_{ET} = k_{QD-SC} - k_{QD}. \qquad (2.19)$$

Further drawbacks have followed; El-Sayed and co-workers showed that the hole can contribute significantly to the visible bleach, preventing the separation of electron and hole dynamics (62). It is also worth noting that investigating the ground state transition bleach would not allow for detection of electron transfer from hot carriers. Ignoring hole cooling, there are further drawbacks, as electron transfer or surface trapping may result in an electric field that, although indicating charge separation, will Stark shift the absorption features complicating the analysis (59). Despite these drawbacks, numerous attempts have been made.

Most notably Kamat and co-workers studied electron transfer from CdSe to TiO_2 nanostructures, reporting electron transfer time scales from 5 to 140 ps (*10*). They claim to observe what they proposed was charge transfer from the hot $1P_e$ but were unable to resolve these dynamics with the time resolution of the experiment (130 fs) and were unable to provide convincing evidence for their claim. Most recently, Zhang and co-workers report sub-picosecond electron transfer lifetimes using CdSe QDs-to-polycrystalline TiO_2 (*63*). This suggests that some of the difficulties in measuring and modeling the multi- and non-exponential behavior of the visible bleach recovery come from the heterogeneity of the high surface area TiO_2 matrix.

Very recently, terahertz pump-probe spectroscopy has been used to measure electron transfer dynamics in PbSe QD-to-SnO_2 nanostructures (*64*). Terahertz spectroscopy measures the time dependant electron density through Drude absorption of free carriers. The authors report electron transfer times of ~100 ps for small QDs and ~1 ns for large QDs. Although the time dependent electron density can be related to charge transfer, it is not a direct signature of a charge separation event.

The range of reported timescales and clear limitations of the TA technique necessitate the use of alternative techniques that can resolve the dynamics of these complex systems, ideally one sensitive to a clear indication of charge transfer. In the following chapters, the proposal and implementation of such a technique is presented.

Chapter 3: Time Resolved Surface Second Harmonic Generation

Second harmonic generation (SHG) is the special case of a general nonlinear process known as sum frequency generation (SFG). SFG is the process by which two photons of frequency ω_1 and ω_2 are converted to one photon of frequency $(\omega_1 + \omega_2)$. Second harmonic generation is merely when $\omega_1=\omega_2$ and the resulting photon has a frequency of 2ω (Fig 3.1).

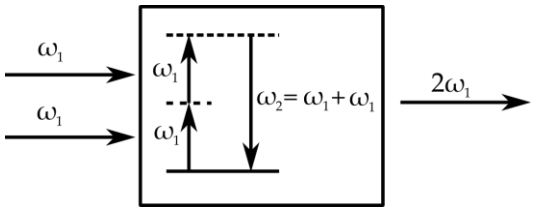

Figure 3.1: Illustration of second harmonic generation, where two photons of frequency ω and converted to one photon of frequency 2ω inside a nonlinear material. Note, the transitions may involve real or imaginary states.

The following chapter describes how a pulsed laser system can be used to measure the femtosecond dynamics of charge carriers by the generation of second harmonic light.

3.1 SECOND HARMONIC GENERATION: THEORETICAL FRAMEWORK

3.1.1 The driven wave

This section is intended to classically demonstrate how a second order nonlinear response can be generated from a pulsed laser. The optical response of a dielectric to an electromagnetic wave $\mathbf{E}(\mathbf{r},t)$ is expressed by the polarization $\mathbf{P}(\mathbf{r},t)$, which is defined as the dipole moment per unit volume. Conventionally, the polarization of the material depends linearly on the strength of the electromagnetic field at any wavelength as follows

$$\boldsymbol{P}(\omega) = \epsilon_0 \chi^{(1)}(\omega)\boldsymbol{E}(\omega) \qquad (3.1)$$

Where $\chi^{(1)}$ is the linear susceptibility. Usually this sufficient to describe how polarization is affected by an EM field, but when the EM field becomes strong enough (highly intense light, such as that produced by a pulsed laser), it is important to use a more generalized expression which expresses polarization as a power series in the field **E**(**r**,t)

$$\boldsymbol{P}(\omega) = \epsilon_0\left[\chi^{(1)}(\omega)\boldsymbol{E}(\omega) + \chi^{(2)}(2\omega)\boldsymbol{E}^2(\omega) + \chi^{(3)}(3\omega)\boldsymbol{E}^3(\omega) \ldots\right]$$
$$\equiv \boldsymbol{P}^1(\omega) + \boldsymbol{P}^2(2\omega) + \boldsymbol{P}^3(3\omega) \ldots \qquad (3.2)$$

Therefore, the overall polarization is equal to the sum of the polarization of the harmonics. Second harmonic generation is governed by $\chi^{(2)}$, otherwise known as the second order nonlinear susceptibility. Because **E**(**r**,t) and **P**(**r**,t) are vector quantities, $\chi^{(1)}$, $\chi^{(2)}$ and $\chi^{(3)}$ are second, third and fourth rank tensors, respectively. As the electromagnetic wave varies over time, one component of the polarization changes at twice the frequency. Given a laser beam with electric field strength

$$\boldsymbol{E}(t) = Ee^{-i\omega t} + c.c. \qquad (3.3)$$

interacting with a material, or material surface with second order susceptibility $\chi^{(2)}$, the second order polarization created would be given by substituting (3.3) into $\boldsymbol{P}^2(t) = \chi^{(2)}\boldsymbol{E}^2(t)$, which is the second order polarization with instantaneous response, to give (*65*),

$$\boldsymbol{P}^2(t) = 2\chi^{(2)}\boldsymbol{E}\boldsymbol{E}^* + \left(\chi^{(2)}\boldsymbol{E}^2 e^{-2\omega t} + c.c.\right). \qquad (3.4)$$

It can be seen that the first term has a contribution at zero frequency and the second term has a contribution at two times the harmonic frequency. Time dependent changes in polarization can drive the formation of electromagnetic radiation (66). It has been determined that changes in polarization are the driving force for SHG, therefore it is important to investigate how EM wave induced changes in the polarization occur for TiO_2.

3.1.2 The role of Symmetry in Nonlinear Susceptibility

In a material possessing inversion symmetry (centrosymmetric), the potential felt by an electron moving in the crystal must be isotropic around an inversion center. Mathematically, this requirement can be expressed simply as $U(x) = U(-x)$. As a consequence, only even order terms are allowed in the potential energy function of Eq. (3.2). Following Boyd (66), this relationship is best explained looking at the polarization of the material.

$$\boldsymbol{P} = \epsilon_0\left[\chi^{(1)}\boldsymbol{E} + \chi^{(2)}\boldsymbol{E}^2 + \chi^{(3)}\boldsymbol{E}^3 + \chi^{(4)}\boldsymbol{E}^{(4)} \ldots\right] \qquad (3.5)$$

In a centrosymmetric material, if the sign of the electric field is changed, the sign of the polarization must also change, but we see that only the odd power terms change signs.

$$-\boldsymbol{P} = \epsilon_0\left[-\chi^{(1)}\boldsymbol{E} + \chi^{(2)}\boldsymbol{E}^2 - \chi^{(3)}\boldsymbol{E}^3 + \chi^{(4)}\boldsymbol{E}^{(4)} \ldots\right] \qquad (3.6)$$

Therefore, for the polarization to be negative, the even order terms must vanish, which will only happen when $\chi^{(2)} = \chi^{(4)} = \chi^{(2n)} = 0$. This means that, within the electric dipole approximation, second harmonic generation is forbidden in the bulk of centrosymmetric media, such as isotropic (gases, liquids and amorphous solids) and centrosymmetric crystalline materials (Si, rutile, sapphire).

When describing the second-order nonlinear optical response far from resonances, the medium is generally taken to be lossless and dispersionless (66). When this is the case, the nonlinear susceptibility is independent of frequency and the notation d_{ijk} is used instead of $\chi^{(2)}_{ijk}$, and is defined by the relation

$$P_i = 2d_{ijk}\, E_j\, E_k\,. \qquad (3.7)$$

Here, d_{ijk} represents the element in the 27-term triad (third rank tensor) which relates the *i*-directed polarization of the nonlinear medium to the *j*- and *k*-polarized incident fields. There is no physical difference in exchanging E_j and E_k in (3.7), the subscripts k and j can be replaced by a single symbol denoting the pieozoelectric contraction (*67*).

$$xx = 1 \quad yy = 2 \quad zz = 3$$
$$yz = zy = 4 \quad xz = zx = 5 \quad xy = yx = 6$$

The resulting d_{ij} tensor can be written in a 3x6 matrix that operates on the **EE** vector to yield the polarization **P**,

$$\begin{bmatrix} P_x \\ P_y \\ P_z \end{bmatrix} = 2 \begin{bmatrix} d_{11} & d_{12} & d_{13} & d_{14} & d_{15} & d_{16} \\ d_{21} & d_{22} & d_{23} & d_{24} & d_{25} & d_{26} \\ d_{31} & d_{32} & d_{33} & d_{34} & d_{35} & d_{36} \end{bmatrix} \begin{bmatrix} E_x^2 \\ E_y^2 \\ E_z^2 \\ 2E_z E_y \\ 2E_z E_x \\ 2E_x E_y \end{bmatrix}. \qquad (3.8)$$

For a centrosymmetric material, all the d_{ij} elements equal zero. For non-centrosymmetric materials, the non-zero elements are determined by the point-group symmetry. For example, cadmium selenide has the wurtzite crystal structure, which has 6*mm* point-group symmetry. If we assign the z-axis as the principal optical axis (c-axis) the resulting d_{ij} matrix (*67*),

$$d^{6mm} = \begin{bmatrix} 0 & 0 & 0 & 0 & d_{15} & 0 \\ 0 & 0 & 0 & d_{24} & 0 & 0 \\ d_{31} & d_{32} & d_{33} & 0 & 0 & 0 \end{bmatrix}. \qquad (3.9)$$

Additionally, $d_{15} = d_{24}$ and $d_{31} = d_{32}$, resulting in only three unique, non-zero terms from an initial twenty-seven. The form of $d^{(6mm)}$ also displays some intuitively expected results. Since it is the polarity/anisotropy of the z-axis (c-axis) in wurtzite that is responsible for broken inversion symmetry, it is not surprising that the x- and y-axes (or any two directions orthogonal to the c-axis) are completely interchangeable. It is also not surprising to find a non-zero $d_{33} = d_{zzz}$ component (all electric fields polarized along the c-axis, which in wurtzite is found to be the largest of the three non-zero terms (*67*).

3.2 SURFACE SECOND HARMONIC GENERATION FROM RUTILE (110)

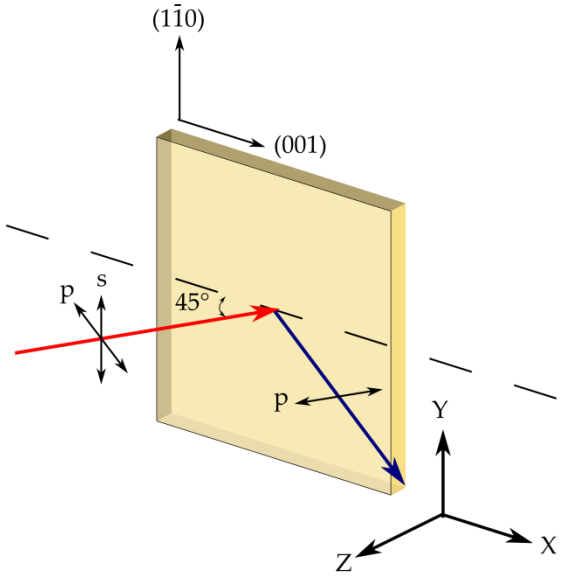

Figure 3.2: Definition of the coordinate system used to describe the nonlinear susceptibility of the TiO_2 rutile (110) surface. The x-coordinate runs along the (001) direction in the surface plane; the y-coordinate runs along the (1$\bar{1}$0) direction in the surface plane; the z-coordinate is the surface-normal (110) direction.

When dealing with the surface nonlinear susceptibility, the elements of the susceptibility matrix are described in terms of a coordinate system relative to the surface normal direction. In this coordinate system, the z-axis is the surface normal and *x* and *y* lie in the surface plane. The $\chi_{zzz}^{(2)surf}$ element of the surface nonlinear susceptibility tensor, which is always allowed due to broken symmetry in the surface-normal direction, is often the strongest contributor (*68*).

For SHG at an azimuthally isotropic interface with an infinite number of mirror planes perpendicular to the surface ($C_{\infty v}$ symmetry), for example, a liquid or amorphous

glass, there are three independent nonzero terms in the surface nonlinear susceptibility tensor. Following the piezoelectric contraction defined earlier (Eq. (3.8)), we write (*69*),

$$\chi_{ijk}^{(2)surf}\{C_{\infty v}\} = \begin{bmatrix} 0 & 0 & 0 & 0 & \chi_3 & 0 \\ 0 & 0 & 0 & \chi_3 & 0 & 0 \\ \chi_2 & \chi_2 & \chi_1 & 0 & 0 & 0 \end{bmatrix}. \qquad (3.10)$$

Where $\chi_2 = \chi_{zxx} = \chi_{zyy}$, $\chi_1 = \chi_{zzz}$, $\chi_3 = \chi_{yyz} = \chi_{yzy} = \chi_{xxz} = \chi_{xzx}$. Surface susceptibility tensors can be defined for each facet of a centrosymmetric crystal. This has been done experimentally for the (110) surface of rutile TiO_2 by Kobayashi et al. (*70,71*). They define their surface coordinate system as shown in Fig. 3.2, from which they found the following three non-zero tensor elements

$$\chi_{ijk}^{(2)surf}\{TiO_2(110)\} = \begin{bmatrix} 0 & 0 & 0 & 0 & \chi_{xxz} = \chi_{xzx} & 0 \\ 0 & 0 & 0 & 0 & 0 & 0 \\ 0 & \chi_{zyy} & \chi_{zzz} & 0 & 0 & 0 \end{bmatrix}, \qquad (3.11)$$

where $\chi_{xxz} = \chi_{xzx}$ is the largest in magnitude, this effect is assigned to the presence of Ti-O zigzag bonds running along the (001) direction of the (110) surface (*71*). By controlling the polarization of the incident light, tensor elements can be selected. Using the surface coordinate system shown in Fig 3.2, *p*-polarized incident light probes the χ_{zzz} and $\chi_{xxz} = \chi_{xzx}$ tensor elements, while *s*-polarized incident light probes only the χ_{zyy} tensor element.

3.3 THE ELECTRIC FIELD-INDUCED SECOND HARMONIC RESPONSE (EFISH)

The electric field-induced second harmonic (EFISH) response at the surface of a centrosymmetric material was first discovered by Lee, Chang, & Bloembergen in 1967 (*72*). SHG, in general, is highly sensitive to slowly varying or dc electric fields because

of the potential for such fields to perturb the symmetry of the medium. Phenomenologically, the EFISH response is treated as a four-wave mixing process modulated by an effective fourth-rank nonlinear susceptibility tensor $\chi^{(3)}_{eff}(2\omega = \omega + \omega + 0)$ that contains contributions from both the surface and the bulk (*73,74*). The total second-order nonlinear (NL) polarization within a semiconductor is given by,

$$\begin{aligned}\mathbf{P}^{NL}(2\omega) &= \mathbf{P}^{BD}(2\omega) + \mathbf{P}^{BQ}(2\omega) + \mathbf{P}^{S}(2\omega) + \mathbf{P}^{EFISH}(2\omega) \\ &= \varepsilon_o \begin{bmatrix} \chi^{(2)}_{bulk}(2\omega) : \mathbf{E}(\omega)\mathbf{E}(\omega) + \chi^{(Q)}_{bulk} : \mathbf{E}(\omega)\nabla\mathbf{E}(\omega) + \ldots \\ \chi^{(2)}_{surf}(2\omega) : \mathbf{E}(\omega)\mathbf{E}(\omega) + \chi^{(3)}_{eff} : \mathbf{E}(\omega)\mathbf{E}(\omega)\mathbf{E}(0) \end{bmatrix}\end{aligned} \quad , \qquad (3.12)$$

where the superscripts BD, BQ, and S refer to bulk dipole, bulk quadrupole, and surface dipole contributions, respectively. For centrosymmetric materials like rutile TiO_2, the BD term vanishes. In the absence of a dc electric field, the BQ and S contributions may be of comparable magnitude, but can be separated by careful control of geometry and polarization (*75*). Such work has been done for the rutile (110) surface of TiO_2 and it was determined that the surface dipole contribution dominates the SH response, especially while controlling the geometry as was done in the following electron transfer studies (*71*). The dominant nonlinear polarization terms reduces to surface dipole and EFISH contributions $\mathbf{P}^{\mathrm{NL}}(2\omega) = \mathbf{P}^{\mathrm{S}}(2\omega) + \mathbf{P}^{\mathrm{EFISH}}(2\omega)$.

The reflected SH field can be divided into the sum of background (surface dipole response when $E^{(\mathrm{dc})} = 0$) and EFISH contributions (*76*)

$$\begin{aligned}\mathbf{E}^{(2\omega)} &= \mathbf{E}_o^{(2\omega)} + \mathbf{E}_{EFISH}^{(2\omega)} \\ &\propto \chi^{(2)}_{surf}\left(E^{(dc)} = 0\right) : \mathbf{E}^{(\omega)}\mathbf{E}^{(\omega)} + \chi^{(3)}_{eff} : \mathbf{E}^{(\omega)}\mathbf{E}^{(\omega)}\mathbf{E}^{(dc)}\end{aligned} \qquad (3.13)$$

For clarity, the linear and nonlinear Fresnel factors have been neglected. The experimentally observed SHG intensity is,

$$\begin{aligned} I^{(2\omega)} &= \left|\mathbf{E}_0^{(2\omega)} + \mathbf{E}_{\text{EFISH}}^{(2\omega)}\right|^2 \\ &= \alpha\left|\chi_{\text{surf}}^{(2)}\right|^2 \left(I^{(\omega)}\right)^2 + \beta\left(\chi_{\text{surf}}^{(2)\,*}\chi_{\text{eff}}^{(3)} + \chi_{\text{surf}}^{(2)}\chi_{\text{eff}}^{(3)*}\right)\left(I^{(\omega)}\right)^2 E^{(\text{dc})} + \gamma\left|\chi_{\text{eff}}^{(3)}\right|^2 \left(I^{(\omega)}\right)^2 \left(E^{(\text{dc})}\right)^2 \end{aligned}$$

,(3.14)

where α, β, and γ are constants that depend on geometry, χ^* is the complex conjugate of χ, and $I^{(\omega)}$ is the incident laser field intensity. Because rutile TiO_2 (110) exhibits a large background SH signal in the absence of an external electric field under the geometry used here (i.e. $\chi_{surf}^{(2)} \gg \chi_{eff}^{(3)}$), the third term in Eq. (3.14) can be neglected. Therefore, the measured SH intensity is linear in the electric field strength,

$$\begin{aligned} I^{(2\omega)} &\approx I_0^{(2\omega)} + \Delta I^{(2\omega)} \\ &\approx I_0^{(2\omega)} + \eta\left(I^{(\omega)}\right)^2 E^{(\text{dc})}, \end{aligned} \qquad (3.15)$$

with η containing nonlinear susceptibilities and geometric factors. If we take the charge-separated Donor-TiO_2 interface to be a parallel plate capacitor, then the electric field strength at the interface due to charge separation is,

$$\begin{aligned} E^{(dc)} \equiv E^{sep} &= \frac{1}{\varepsilon_r \varepsilon_o}\frac{2Q^{sep}}{A}, \\ &\propto Q^{sep} \end{aligned} \qquad (3.16)$$

where Q^{sep} is the amount of separated charge. As a result, we expect the EFISH signal to scale approximately linearly with Q^{sep},

$$\Delta I^{(2\omega)} \propto Q^{sep}. \qquad (3.17)$$

3.4 TIME RESOLVED SECOND HARMONIC GENERATION: EXPERIMENTAL IMPLEMENTATION

3.4.1 Optical layout

The experimental set-up for the TR-SHG experiment is illustrated in Figure 3.3. A home-built 80 MHz Ti:sapphire oscillator, with a central wavelength at 820 nm, pulse duration of 35 fs, 40 nm bandwidth at FWHM, with an output power of 400mW, is used to seed a regenerative amplifier operating at 250 kHz, at 810 nm central wavelength, with a 50 fs pulse duration, 20 nm FWHM, with an output power of 1,300 mW (Coherent, RegA 9050). The output beam is then split into two paths. One path (the pump) can either be directed into an infrared optical parametric amplifier (950-1600 nm), a visible optical parametric amplifier (450-750 nm) or bypass the amplifiers, any of these options can be used to pump the sample at controllable energies. The other path (the probe) is directed along a variable length delay before being spatially and temporally overlapped on the sample surface. The polarization of each path can be independently controlled allowing for the selective measurement of different non-linear susceptibility tensors. Long-pass filters are placed immediately in front of the cryostat (Janis ST-100), where the sample is housed, to remove any second harmonic light generated from the laser or any optical components in the beam path. The cryostat windows are made of Suprasil II, a high-quality amourphous silica glass, transparent to the second harmonic light and having a

negligible second order nonlinear susceptibility at normal incidence. Pump and probe beams are focused non-collinearly at a low mutual angle (<5°), to allow for spatial separation of the reflected beams, but provide acceptable phase matching at the sample surface. The laser spot size is kept at approximately a 260 μm x 360 μm ellipse, as measured by knife edge technique. The entire sample housing and signal detection path are kept in a dark housing to reduce detection of spurious light.

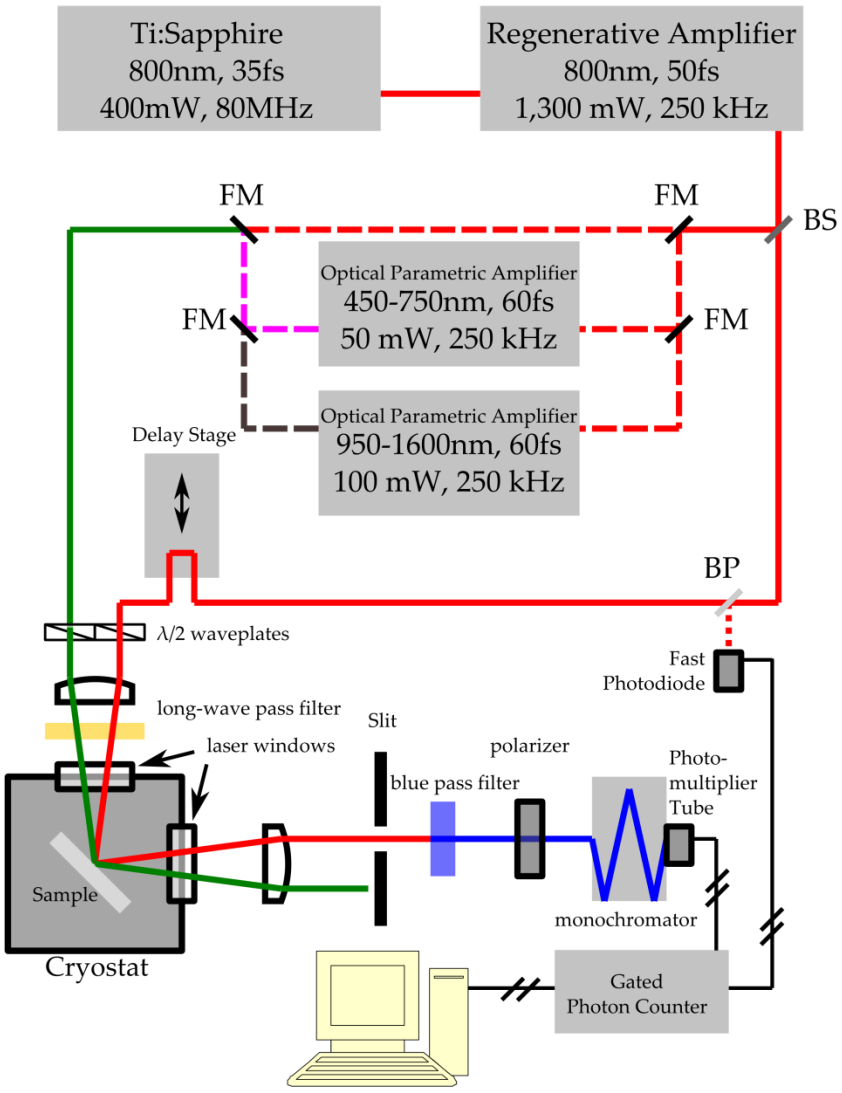

Figure 3.3: Schematic of the optical setup for time-resolved second harmonic generation (TR-SHG) built by the author. Colored lines indicate the path of laser light; dashed lines are optional paths the beams may take configurations of the experiment; the green line represents any arbitrary wavelength of light. Thin black lines with hashes denote electronic data pathways. The sample is housed within a controlled-atmosphere cryostat (Janis ST-100). λ/2 waveplates control the linear polarization state of the input beams and a polarizer selects which polarization of the SHG signal is detected. SHG photon detection is accomplished with a photomultiplier tube (Hamamatsu R4220P) whose output is fed to a photon counter (Stanford Research SR400). A personal computer records the data and coordinates movement of the delay stage. BS=beamsplitter; FM=flip mirror; BP=beam pick-off.

By conservation of momentum, second harmonic (SH) light generated from the sample surface is collinear with each reflected beam. When pump and probe pulses are overlapped on the sample in space and time, a third nonlinear signal at the sum of the two frequencies (sum-frequency, SF) is generated at a wave vector in between the two reflected SH signals, as shown in Fig 3.4. This SF signal is equivalent to the cross-correlation of the pump and probe laser pulses and provides an internal reference for optimizing spatial overlap, minimizing pulse width, and determining the delay at which pump and probe pulses arrive at the sample surface at the same time.

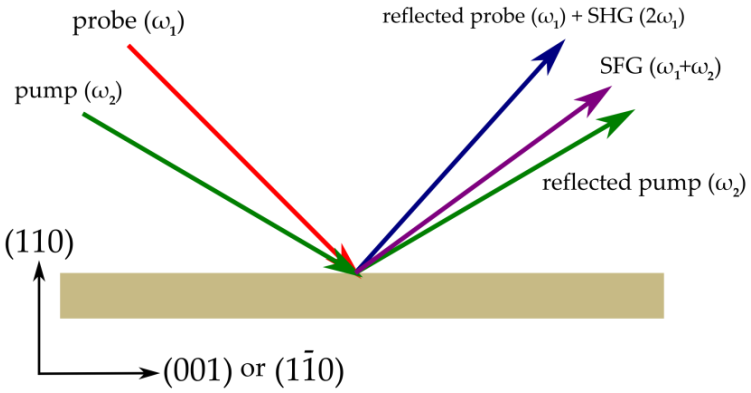

Figure 3.4: Illustration of the beam paths at the sample surface. When pump and pulse are overlapped in time and space, a sum frequency signal is generated, which is spatially separated from the reflected pump, probe and SHG signal due to conservation of momentum.

When using independent colors for pump and probe beams, it is possible that other nonlinear processes can generate light at the same frequency as the SH signal. One process that has been observed to do this is degenerate four-wave mixing (DFWM), where two photons combine, while the energy of a third photon is lost, resulting in a photon of energy $E = \omega_1 + \omega_1 - \omega_2$. This process is illustrated on the right side of

Figure 3.5 next to second harmonic generation (Left). DFWM can interfere with SH collection when $E^{pump} \sim {}^{3}/_{2}\, E^{probe}$.

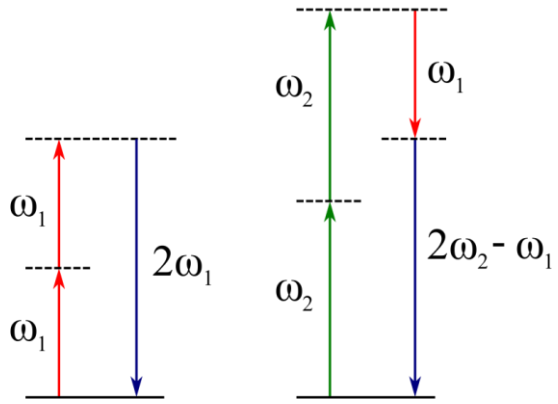

Figure 3.5: Schematic of SHG (left) and DFWM (right) where the generated photons have the same energy ($\omega_2 = 3/2\omega_1$).

3.4.2 Data Acquisition

Second harmonic light generated at the sample surface is many orders of magnitude less intense than the reflected probe beam that travels collinear. To separate this light, the beam is directed using dielectric mirrors that are highly reflective to the SH frequency and transmits the fundamental frequency (Layertec GmbH), then passed through a blue pass filter with high optical density at the fundamental frequency (SCHOTT, BG39). The filtered light is then directed into a 1/8 m monochrometer (Oriel Cornerstone) attached to a high work function photon counting photomultiplier tube (PMT) (Hamamatsu, R4220P).

PMTs have high gain and sensitivity but suffer from many forms of noise. Photon counting eliminates noise from the high gain by discriminating each pulse and digitizing the signal into integer counts. To limit the number of false counts collected, gated photon counting is employed. A fast photodiode generates an electrical gate

whenever a laser pulse is detected. Only counts recorded during a short time window correlated to when a pulse would have hit the sample surface register a count. The regenerative amplifier operates at 250 kHz, equating to 4 μs between pulses. The signal pulse duration from the PMT is 20 ns, making the duty cycle of the experiment 0.005. By gating the detection with a 20 ns gate, 99.5% of the dark counts are filtered.

One limitation to gated photon counting is that by discriminating the signal, only one count can be registered per pulse. The sampling of discrete events, such as single photon detection, observes Poisson statistics. To avoid collecting multiple photons per pulse, the count rate should be kept below 1% of the repetition rate.

Chapter 4: Understanding the Bathochromic Shift of Exciton Transitions in 2-Dimensional arrays of PbSe Quantum Dots

Much of the content of this chapter have been published as:

> K. J. Williams, W.A. Tisdale, K.S. Leschkies, G. Haugstad, D.J. Norris, E.S. Aydil, and X.-Y. Zhu, "Strong Electronic Coupling in Two-Dimensional Assemblies of Colloidal PbSe Quantum Dots", *ACS Nano* **3**, 1532 (2009)
>
> A. Wolcott, V. Doyeux, C. Nelson, KW Lei, R. Gearba, K. Yager, A. Dolocan, K. Williams, and XY. Zhu, "An Anomalously Large Polarization Effect is Mainly Responsible for Excitonic Redshifts in PbSe Quantum Dots Solids", *J. Phys. Chem. Lett.,* **2**, 795-800 (2011)

In this chapter, we detail the changes in structural and optical properties of condensed 2-D and 3-D semiconducting nanocrystal films. We investigate the effects of removing or replacing large capping ligands. We determine, through the use of atomic force microscopy (AFM), scanning electron microscopy (SEM), grazing incidence wide-angle x-ray scattering (GIWAXS), that inter-particle distance is reduced, consistent with the removal and exchange of long chain capping ligands. Fourier transform near infrared (FT-NIR) spectroscopy reveals bathochromic (red) shifts in the in the first exciton of chemically treated 2-D and 3-D QD arrays. These changes are attributed to enhanced "geometric frustration" in 3-D films, as well as anomalously large "solvatochromism".

4.1 INTRODUCTION

If solid-state semiconductor materials are to keep pace with emerging organic alternatives, both in cost and large area flexible design, they will need to take advantage of low cost solution processing techniques such as, roll-to-roll transfer, dip coating, spin coating, or inkjet printing. Colloidal semiconductor nanocrystals, or quantum dots (QDs), are attractive for these applications because of the ease with which their material, optical and electronic properties can be controlled (*30,31*). Moreover, they can be processed from solution to form high quality ordered assemblies known as superlattices

(*77,78*). These benefits also mean that such materials provide a unique model system for the study of fundamental physical processes, such as charge carrier transport, exciton diffusion, and energy transfer.

Consequently, a number of studies have explored charge transport in thin films of colloidal QDs (*79-84*). However, the presence of long-chain surface ligands, which are required for the synthesis, colloidal stability, and surface passivation of the QDs, leads to poor conductivity in the films due to weak inter-QD electronic coupling. Therefore, much recent effort has focused on increasing the electronic coupling in such films to improve their conductivity.

A number of studies have explored the removal or exchange of capping molecules to increase inter-QD electronic coupling. Examples include the drying of quantum dot thin films and the partial evaporation of weakly bound capping molecules (*85,85*), the chemical removal of capping molecules via reduction (*87*) or oxidation (*88*), the thermal desorption/decomposition of capping molecules under vacuum or inert conditions (*51*), and the exchange of bulky or long ligands by small ones (*89*,*90*). A significant increase in the conductivity was demonstrated when the surface ligands were replaced by shorter molecules and charge carriers were electrochemically injected into the QDs (*89*). Later it was shown that, even without the injection of extra carriers, the conductivity of films of PbSe QDs could be increased by as much as 10 orders of magnitude if films were exposed to a solution of hydrazine (*90*).

This dramatic increase in conductivity has been attributed to the partial removal of oleic acid ligands from the surface of the PbSe nanocrystals, resulting in decreased inter-QD spacing and increased inter-QD electronic exchange coupling. This was supported by the observation that the first exciton absorption peak shifted red by $\Delta E_{EX}^{1} \approx 20\, meV$ after immersion in 1 M hydrazine in acetonitrile. Subsequent work has

examined the structural, optical, and electronic changes in PbSe QD thin films that are exposed to a variety of thermal and chemical treatments in more detail (*91,92*). The observed variations included red shifts in the first exciton absorption peak of 12 meV and 27 meV following treatment with 1 M hydrazine in acetonitrile and in ethanol, respectively. After these hydrazine treatments, it was also verified that the size of the PbSe QDs did not change, but the inter-QD distance decreased. Thus, these results support the initial claim that the red shift in the exciton transition occurs due to a decrease in the inter-QD spacing. This can cause (i) an increase in the average dielectric constant of the film, solvatochromically stabilizing the exciton, (ii) an increase in the inter-QD radiative coupling, and (iii) an increase in the inter-QD electronic coupling.

4.2 EXPERIMENTAL DETAILS

4.2.1 Sample Preparation

Colloidal PbSe nanocrystals were synthesized based on methods developed by Murphy et al. (*93*) and Luther et al. (*92*). In a typical synthesis, PbO (2.5 g), oleic acid (OA, 9 mL), and 1-octadecene (35 mL) were placed in a three-neck round-bottom flask. The reaction flask was then degassed to <40 mTorr while stirring vigorously and purged with dry nitrogen gas. The degassing process was repeated three times. The reaction vessel was heated to 180 °C under nitrogen and was maintained at that temperature for approximately 1 hr while the precursor solution turned optically clear. Meanwhile, a solution of Se dissolved in trioctylphosphine (TOPSe; 1.0 M, 21 mL total volume) was prepared and loaded into syringes inside a nitrogen glovebox. 15 mL of cold (0°C) anhydrous toluene was loaded into separate syringes. The TOPSe precursor was removed from the nitrogen glovebox and immediately injected into the reaction vessel. The temperature of the reaction solution was maintained at 150 °C during nanocrystal growth.

UV/visible/near-infrared absorption measurements (Cary 5E) were used to monitor nanocrystal growth. Once the desired nanocrystal size was obtained (growth time varied from 30 s to 10 min), the heat source was removed from the reaction vessel and 15 mL of anhydrous toluene was swiftly injected into the vessel. The reaction vessel was rapidly cooled to room temperature using an ice bath. The reaction product was cannulated from the reaction vessel into a Schlenk flask and transferred into the nitrogen glovebox.

All post-synthesis methods necessary to prepare clean nanocrystal dispersions were carried out in the nitrogen glovebox. The PbSe nanocrystals were precipitated out of the growth solution using a mixture of anhydrous methanol, butanol, and 200 proof ethanol (1:1:2, respectively) and isolated after centrifuging. The supernatant was discarded and the nanocrystals were re-dispersed in dry hexane. Precipitation with 200 proof ethanol followed by re-dispersion in dry hexane was repeated three times. The final product was a solution (variable concentration) of oleic acid-capped PbSe nanocrystals (OA-PbSe) in hexane.

Single crystal rutile TiO_2 was purchased from MTI Corporation (Richmond, CA). The (110) oriented crystals were 10 mm x 10 mm square, 1 mm thick, and mechanically polished on both sides. In-plane crystallographic orientation was determined by optical birefringence at 532 nm. Atomically flat surfaces were obtained by successive rinsing with 0.2 M NaOH then deionized water, followed by immersion in 1 M HCl under UV irradiation (254 nm) for 30 min and finally rinsing with deionized water and acetone in air (*94*).

All PbSe nanocrystal films were prepared in a controlled atmosphere argon glovebox to prevent PbSe oxidation. Clean substrates were rinsed with distilled hexane before partial submersion in the OA-PbSe/hexane solution followed by withdrawal at a constant velocity of 1 cm/s. Desired coverage of the TiO_2 substrate was achieved by

varying the concentration of the OA-PbSe/hexane solution (typically ~5 mg/mL) and verified by atomic force microscopy (AFM). The dip-coating process yielded samples that were optically uniform over a large area in the center of the substrate with drying lines visible at the top of the sample and along the edges.

Ligand exchange reactions were carried out using solutions of the following small molecules in acetonitrile: hydrazine (HYD); 1,2,-ethanedithiol (EDT or C2); 1,3-propanedithiol (PDT or C3); 1,4-butanedithiol (BDT or C4); 1,5-pentanedithiol (PDT or C5); 1,6-hexanedithiol (HDT or C6); 1,8-octanedithiol (ODT or C8). The solution concentrations were 1 M for hydrazine and 0.1 M for the dithiol molecules. Samples were submerged in the ligand exchange solutions until there were no further changes to the ATR-FTIR spectra.

4.2.2 Characterization Techniques

4.2.2.1 Atomic Force Microscopy

Atomic force microscopy (AFM), scanning electron microscopy (SEM) and grazing incidence wide angle x-ray scattering (GIWAXS), were used to determine coverages and investigate morphological changes in monolayer PbSe films following ligand exchanges. AFM was carried out in a humidity-controlled (≤ 5% RH) Agilent 5500 scanning probe microscope operating in open loop. A silicon tip integrated with a rectangular, uncoated silicon cantilever (Applied Nanostructures, < 10 nm radius of curvature, 3 N/m nominal spring constant, resonance frequency of ≈70 kHz, and quality factor of ~140) was used in AC mode. Operation under low humidity and in AC mode with the oscillator in the net attractive regime was necessary to prevent transfer of nanocrystals to the silicon tip or otherwise disturb the PbSe film.

4.2.2.2 Attenuated Total Internal Reflection Fourier Transform Infrared (ATR-FTIR)

ATR-FTIR spectroscopy measurements were carried out in a nitrogen glovebox on a Nicolet 6700 FTIR-NIR spectrometer with both a liquid nitrogen cooled mercury doped cadmium telluride (MCT) detector and an indium doped gallium arsenide (InGaAs) detector. IR light was directed through the waveguide, generating an evanescent wave at the surface of the waveguide. The distance this evanescent wave extends beyond the crystal surface is determined by the following equation.

$$d_p = \frac{\lambda}{2\pi\sqrt{\eta_1^2 Sin^2\theta - \eta_2^2}}, \qquad (4.2)$$

where λ is the wavelength of light, η_1 is the refractive index of the waveguide and η_2 is the refractive index of the surrounding medium. By increasing the number of reflections, the effective path length is increased, increasing the sensitivity by $\sqrt{n_{reflection}}$. Waveguides used for attenuated total internal reflection Fourier transform infrared (ATR-FTIR) spectroscopy measurements were made from Rutile (110) single crystals purchased from Princeton Scientific that were cut to 32 mm x 10 mm rectangular, 1 mm thick, and mechanically polished on both sides. The ends were polished at 45° creating a parallelogram, an illustration of the waveguide and optical path of the infrared light can be seen in Figure 4.1.

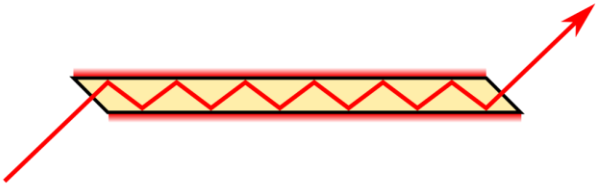

Figure 4.1: Illustration of attenuated total internal reflection, note the evanescent wave at the surface of the waveguide.

4.2.2.3 Scanning Electron Microscopy (SEM)

SEM was performed on a Hitachi S-5500 on both carbon coated Cu grids (#01834) and on Si3N4 windows (Ted Pella Inc., Redding, CA.). Samples were drop cast onto Cu grids under open-air conditions or dip-coated onto Si_3N_4 membranes inside the glovebox.

4.2.2.4 Grazing-incidence wide-angle x-ray scattering (GIWAXS)

GIWAXS measurements were performed at the X9 end-station at the National Synchrotron Light Source (NSLS), Brookhaven National Laboratory. Two-dimensional scattering images were acquired using an area detector, positioned at ~200 mm from the sample, and with an x-ray wavelength of 0.0873 nm (photon energy of 14.20 keV). The samples were investigated at an angle of incidence of 0.1°, 0.2° and 0.4°. Data conversion to q-space was accomplished by measuring a standard sample with known scattering features (Silver Behenate). The incident beam was collimated by slits, and focused onto the sample position by a KB mirror system; the beam size at the sample position was approximately 100 μm in width, and 80 μm in height. Integration of the GIWAXS data was performed with a CYGWIN based data analysis software package on a PC.

4.2.2.5 Size Calibration

Nanocrystal size is reported either by direct measurement with SEM, or by calibration with the energy of the first peak in the optical absorption spectrum following the calibration curve determined by Dai et al. (*95*), by the equation

$$D = \frac{(\lambda - 143.75)}{281.25} \qquad (4.1)$$

where λ is the wavelength of the first exciton transition.

4.3 THE EFFECTS OF LIGAND REMOVAL WITH HYDRAZINE

4.3.1 Structural Changes

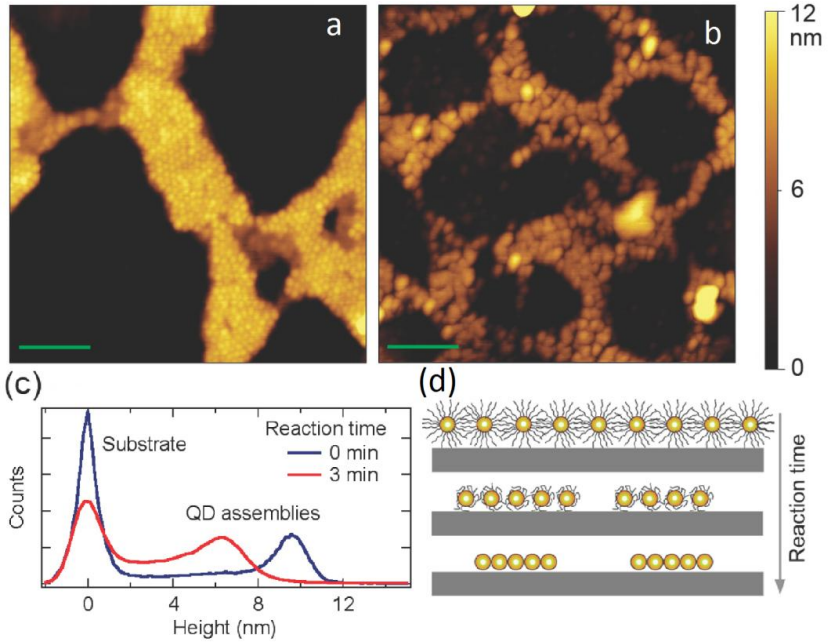

Figure 4.2: Attractive-regime AC-mode atomic force microscopy (AFM) images of submonolayers of PbSe QDs (5.7 nm) assembled on TiO 2 (110): (a) as-deposited QDs with oleic acid surface ligands; (b) after exposure to 1 M hydrazine in acetonitrile for 3 min. Green scale bars are 100 nm. (c) Height histograms of images (a) and (b). The cartoon illustrates proposed morphology changes with reaction time.

Figure 4.1 shows atomic force microscopy (AFM) images of a sub-monolayer of PbSe QDs on a (110) TiO_2 surface taken before and after the hydrazine exposure (3 min). Before exposure (Figure 4.2a), the surface is characterized by a network of two-dimensional islands. Figure 1a clearly reveals hexagonally close-packed domains with an inter-QD distance of 10 ± 1 nm. This is also the height of the islands, as shown by the blue histogram in Figure 1c. The inter-QD distance and the island height are consistent with the diameter ($\phi = 6\,nm \pm 5\%$) of the QDs plus a 2 nm surface layer due to the oleic acid ligands. After hydrazine exposure, the AFM image (Figure 4.2b) reveals two

effects. First, as shown by the red histogram in Figure 4.2c, the island height decreases to 6 ± 1 nm, which is identical to the size of bare QDs (i.e., without their surface ligands). Second, individual QDs can no longer be resolved in the images. Both effects would be expected if the oleic acid ligands are removed and the inter-QD separation decreased.

The removal of the oleic acid is also verified by vibrational spectroscopy (discussed below). Instead of individual QDs, Figure 4.2b shows larger domains (lateral size 20-40 nm) that are separated by channels. This behavior is consistent with two-dimensional densely packed islands of QDs that suddenly lose their surface ligands while exhibiting limited mobility on the substrate. In this case, the large islands would break up into domains. Our data would then suggest that these domains correspond to 2-D aggregates of 10-100 closely packed bare QDs. We estimate that the surface coverage of these 2-D aggregates in our sample is 20-30% of a monolayer (ML). Note that, after hydrazine treatment, we also see a broadening of the height distribution (Figure 4.2c). This is consistent with the presence of more disorder in the 2-D assemblies and the breakup of large islands as oleic-acid capping molecules are removed. For small domains on the order of or smaller than the tip size, convolution of tip shape with the topography of the 2-D aggregates (including some individual QDs) tends to smear out and broaden the height distribution in a topographical AFM image.

4.3.2 Energetic and Optical Changes

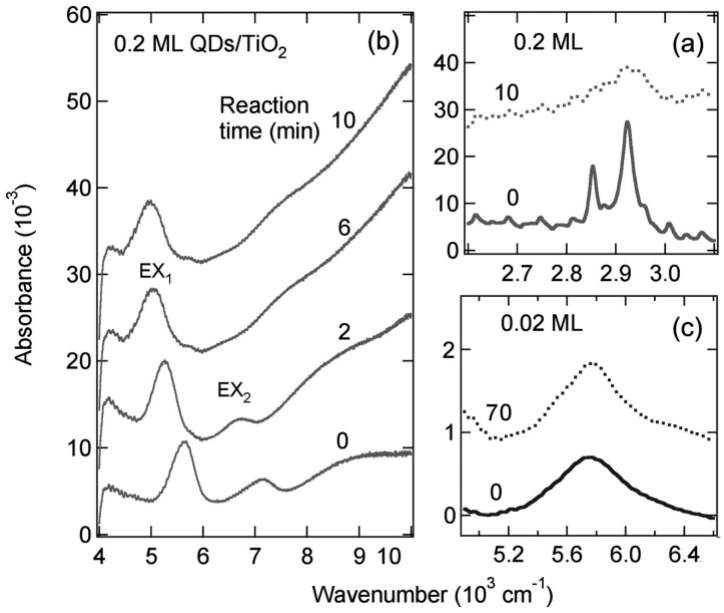

Figure 4.3: (a) ATR-FTIR spectra in the C-H stretch region of a ~0.2 ML film of oleic-acid-capped PbSe QDs (6 nm) on TiO_2 before (solid line) and after (dotted line) exposure to 1M hydrazine in acetonitrile for 10 minutes. (b) ATR-FTIR spectra in the exciton region (EX 1 and EX 2 label the first and second exciton transitions, respectively) of the same surface as a function of reaction time in 1 M hydrazine in acetonitrile. (c) ATR-FTIR spectra of ~0.02 ML oleic acid capped PbSe QDs on TiO_2 (solid) and after exposure to 1M hydrazine in acetonitrile for 70 minutes (dotted).

Additional information can be obtained from ATR-FTIR spectra on similar films. The hydrazine exposure induces two major changes. First, the C-H stretch at ~2920 cm^{-1} (362 meV) disappears (Figure 3.3a), consistent with removal of oleic acid. The residual and poorly resolved C-H stretch that remains may be attributed to background contaminants, as it is also present in the spectrum from a clean TiO_2 surface. Second, a systematic red shift in the first exciton peak with increasing hydrazine exposure time is observed (Figure 3.3b). For ~0.2 ML of 6 nm PbSe QDs on TiO_2, this peak shifts from 5650 cm^{-1} (700 meV) to 5000 cm^{-1} (620 meV) after 10 min of exposure to 1 M hydrazine

in acetonitrile. This shift is independent of the nature of the substrate surface, as a nearly identical shift is observed for the same coverage of PbSe QDs assembled on the SiO_2-terminated Si surface. However, the red shift is not observed when the starting coverage of PbSe QDs is significantly lower, as shown in Figure 4.3c for 0.02 ML after hydrazine exposure for 70 min. Finally, the magnitude of the red shift depends on the size of the QDs. For smaller QDs of ϕ = 4 nm, the maximum red shift is almost twice as large as that of ϕ = 6 nm.

Note that hydrazine treatment of the 0.2 ML samples also increases the absorbance at energies higher than the first exciton transition (Figure 3.3b). This has been observed before for multilayer PdSe thin films and was attributed to enhanced electronic exchange coupling between QDs (*91,92*), although changes in light scattering may also play a role. The results of the ATR-FTIR data on hydrazine treated submonolayer QD films are summarized in Figure 4.4 below.

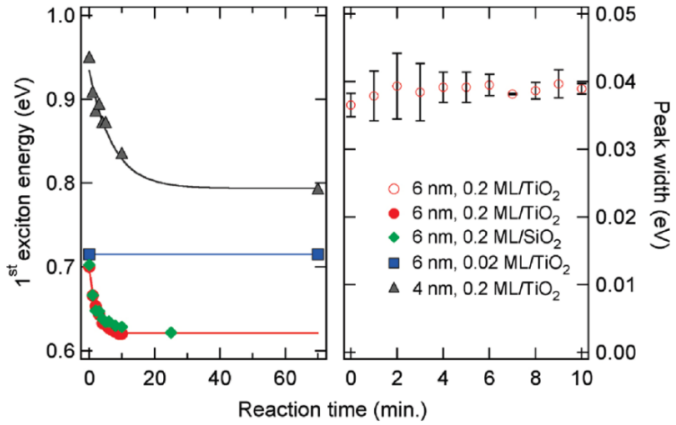

Figure 4.4: Right: width of the first exciton absorption peak as a function of the exposure time to 1 M hydrazine for 0.2 ML of 6 nm QDs on TiO_2. Left: Energy of the first exciton transition as a function of the exposure time to 1M hydrazine in acetonitrile for the indicated surface coverage and QD diameter (red: 0.2 ML of 6 nm QDs, blue: 0.02 ML of 6 nm QD, grey: 0.2 ML of 4 nm QDs) on SiO_2 (green) and TiO_2 (all other colors).

The left panel in Figure 4.4 summarizes the observed shift of the first exciton transition energy as a function of reaction time for ~0.2 ML of 4 nm QDs on TiO_2 (gray triangles), ~0.2 ML of 6 nm QDs (red circles on TiO_2 and green diamonds on SiO_2-terminated silicon), and ~ 0.02 ML of 6 nm QDs on SiO_2 (squares). For the low surface coverage (0.02 ML), the exciton transition energy does not change with hydrazine exposure time. For the high surface coverages (0.2 ML), the exciton transition energy as a function of exposure time can be described well by an exponential decay (solid curves) for both sizes and most of the shifts occur within the first 10 min of reaction time. In contrast to peak position, width of the first exciton absorption peak increases only slightly following hydrazine treatment (10% increase), as shown in the right panel for 6 nm PbSe QDs. The right panal in Figure 4.4 shows the change in full width at half maximum (FWHM) of the first exciton transition. No broadening is observed over the entire duration of the hydrazine treatment.

Comparing 2-Dimensional and 3-Dimensional films, we see the red shift in the first exciton transition is much smaller when the thickness of the QD film is more than one monolayer. Figure 4.5 shows FTIR spectra of a 20 nm thick film of PbSe QDs (diameter slightly less than 6 nm) deposited on the SiO_2 surface. With increasing time of hydrazine exposure, we see up to 80% loss of oleic acid ligands for a total reaction time of 60 min (left panel). The first exciton transition red shifts by a total of 204 cm^{-1} (25 meV), right panel. This red shift is a factor of 3- 4 smaller than that for the submonolayer coverage. This indicates that 2-Dimensional films are able to pack closer, increasing the overall red shift. In order to pack closer, 2-D films do not have to contract in as many dimensions. This lack of geometric frustration allows 2-D films to achieve closer packing and increased excitonic red shifts.

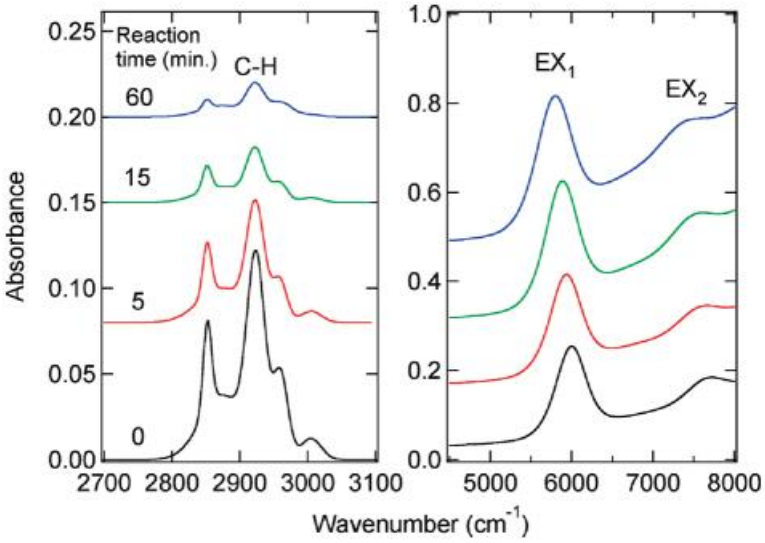

Figure 4.5: ATR-FTIR spectra for a 20 nm thick film of oleic-acid-capped PbSe QDs (~6 nm diameter) on SiO2 as a function exposure time to 1M hydrazine in acetonitrile for 0-60 minutes. The panel on the left shows the C-H stretch region; the panel on the right shows the region near the first (EX 1) and second (EX 2) exciton transitions. The red-shift for this thicker film (~200 cm-1; 25 meV) is 3-4 times smaller than what is observed in monolayer films for similar QD sizes.

4.4 THE EFFECTS OF LIGAND EXCHANGE WITH DITHIOLS

Following the work of Luther et al. (*92*), dried OA-PbSe films were submerged in solutions of 0.1 M dithiols in acetonitrile for 30 s at room temperature then dried under argon. XPS reveals the presence of sulfur within the dithiol-treated PbSe films, supporting the conclusions of Luther et al. that dithiols quantitatively replace OA.

4.4.1 Structural Changes

The SEM images of several dithiols with different length carbon chains (C18, C8, C6, C4, C3 and C2) can be seen in Fig. 4.6. It can be seen that QDs segregate into domains. As the carbon chain length decreases the packing changes from hexagonal to a square lattice.

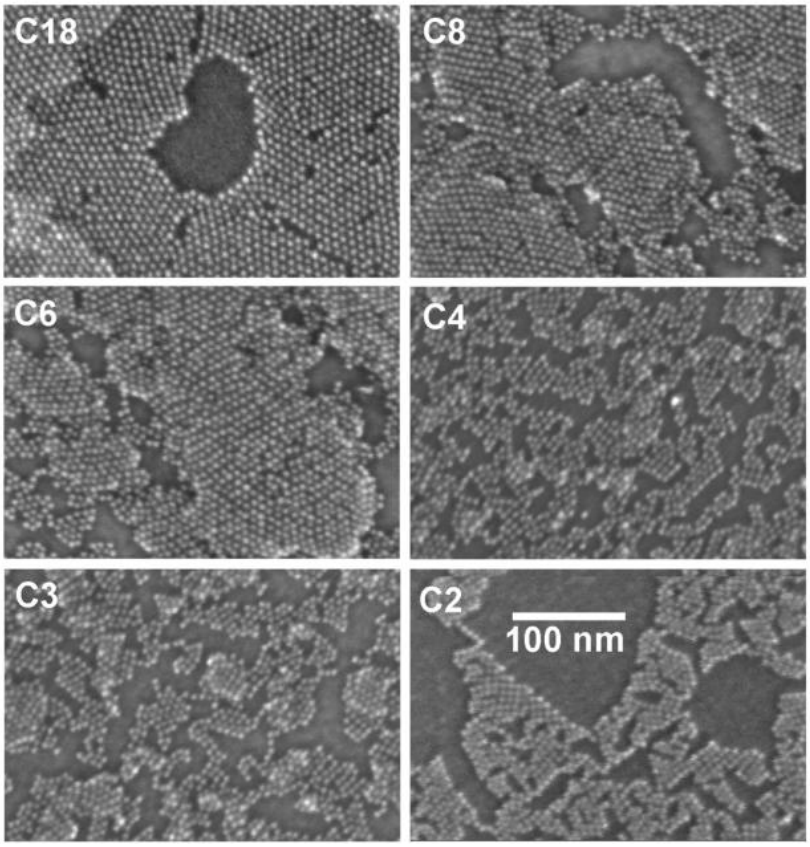

Figure 4.6: SEM images of ~1 ML of PbSe QDs (D = 5.4) on SiO_2 substrates. The QDs are capped with the following molecules: oleic acid (C18), octanedithiol (C8), hexanedithiol (C6), butanedithiol (C4), propanedithiol (C3), and ethanedithiol (C2).

Figure 4.7 shows, as a function of capping molecule length, the measured inter-QD distance (d), which is defined as the edge-to-edge nearest-neighbor distance based on a QD diameter of $5.4 \pm 0.3\ nm$. Here, the data obtained from GIWAXS analysis (0.5 and 2.5 ML) and those from autocorrelation function analysis of SEM images (0.5 ML) were in good agreement. For films of OA-capped QDs, the average inter-QD distance of $d = 2.6 \pm 0.3\ nm$ was far less than the ~4 nm value expected from the sum of two completely packed OA capping layers. In contrast, the OA shell on each QD is not believed to be close-packed, resulting in significant intercalation of the OA molecules

between adjacent QDs. When the OA molecules were replaced by alkanedithiols, the inter-QD distance was consistently longer than the fully stretched molecular length in each case, indicating that intercalation rather than a single molecule bridge dominates.

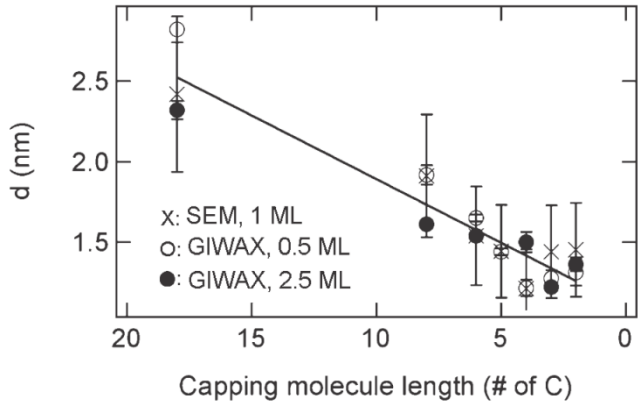

Figure 4.7: Inter-QD distance (edge-to-edge) as a function of capping molecule length (number of -C- units) obtained from autocorrelation functions of SEM images (crosses, submonolayer) and GIWAXS analysis (open and solid circles for 0.5 and 2.5 ML, respectively). The solid line is a linear fit;

4.4.2 Energetic and Optical Changes

Having established the structure and inter-QD distance in the QD thin films, we can relate this information to changes in the electronic structure determined by the optical absorption of the QDs. The nearly complete exchange of OA molecules by alkanedithiols was verified by the decreasing C-H stretch vibrational peak area with decreasing alkanedithiol molecular length; within experimental uncertainty, the integrated C-H stretch peak area was proportional to the number of CH_2 repeating units in each molecule, indicating that the carbon chains are replaced by the shorted molecules.

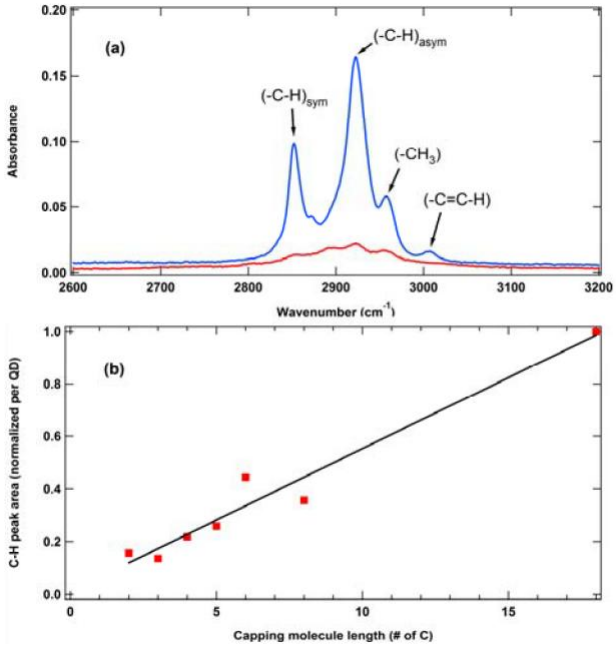

Fig. 4.8: (a) FTIR spectra of a submonolayer PbSe QD thin film before and after exchange of OA capping molecules by C2 for a reaction time of one minute. (b) Integrated C-H stretch peak area (black squares) as a function of capping molecule length together with a linear fit.

Figure 4.9 shows the attenuated total reflectance Fourier transform infrared (ATR-FTIR) absorption spectra a submonolayer (~0.5 ML) QD film with OA and dithiol capping molecules. An increasing redshift in the first exciton is observed as the carbon chain length decreases.

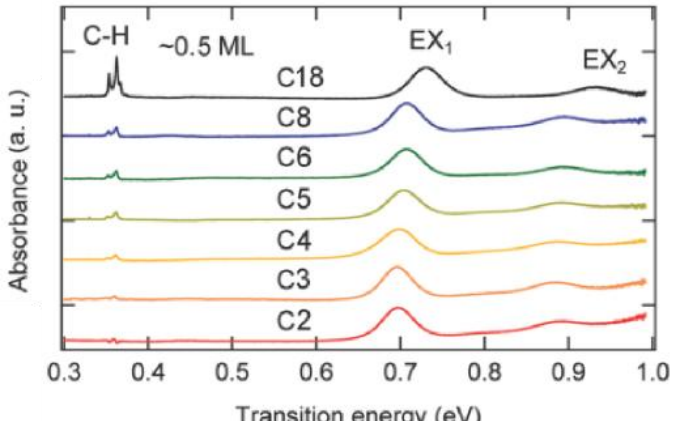

Figure 4.9: ATR-FTIR spectra for submonolayer (~ 0.5 ML,) QD thin films with OA and various dithiol capping molecules. EX 1 and EX 2 denote the first and the second exciton transitions, respectively. C-H: denotes the C-H stretch vibrational transitions.

A summary of the red shifts of the first exciton peak can be seen in Figure 4.10. Within experimental uncertainty, we see no significant difference between the data set for the monolayer (open triangles) and that of the multilayer (solid triangles). Using different substrate materials (SiO_2 and TiO_2) no measurable difference in the magnitudes of red shift was observed. The dashed and dotted lines are theoretical predictions, as detailed in section 4.5. The magnitude of the observed red shift in submonolayer films increased linearly from $22.3 \pm 0.1\, meV$ for 1,8-octanedithiol (C8) to $32.1 \pm 1\, meV$ for 1,2-ethanedithiol (C2).

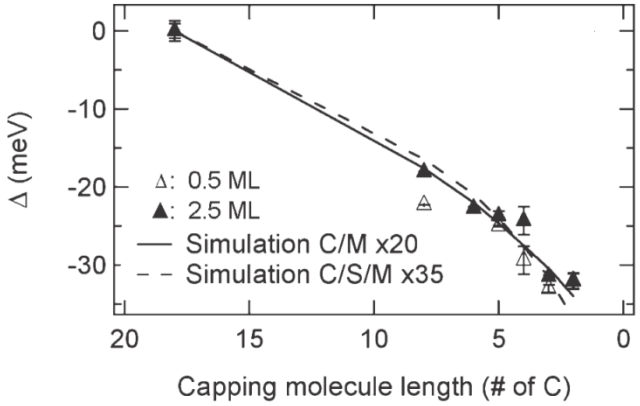

Figure 4.10: Red shifts in the first exciton transition with respect to the OA-capped QDs as a function of capping molecule length (number of -C- units) for 0.5 (open triangles) and 2.5 ML (solid triangles) QD coverage. The solid and dashed lines (scaled by x20 and x35, respectively) are simulations, as detailed in section 4.3.

4.5 ORIGIN OF THE EXCITON RED SHIFT

It has been determined that chemical treatments have caused a decrease in the inter-particle distance, resulting in red shifts in the first exciton transition. There are several possible explanations for the red-shift of the first exciton transition energy following treatment of the PbSe QD film with hydrazine or EDT. One possibility is that the chemical treatment causes QD growth, resulting in smaller quantum confinement and a narrower band gap. This explanation can be eliminated because growth of one QD can only occur at the expense of another. Such a ripening mechanism would lead to a broadening of the first exciton transition, which is not observed (Figure 4.4, right). Law et al. also arrived at the same conclusion following their studies of hydrazine treatment of PbSe nanocrystals (*91*). A second possible explanation, which would account for the large difference in the magnitude of the red-shift between monolayer and multilayer QD films, involves strong QD-substrate electronic interactions. This, too, can be eliminated as a possibility because the magnitude of the red-shift is independent of substrate

material. This is particularly significant for the case of SiO_2, where PbSe electron and hole energy levels reside deep within the SiO_2 band gap, negating the possibility of strong adsorbate-substrate electronic interactions. Additionally, we observe no red-shift for low-coverage (isolated) QDs (Figure 6.4c), suggesting that the interaction responsible for the red-shift is between neighboring QDs.

A third possible explanation for the red-shift of the first exciton transition energy is solvatochromism (further discussion, and illustration, can be found in chapter 2). Solvatochromism, or the dependence of the energy of an optically excited state on the dielectric constant of the solvent, can qualitatively account for most of our observations, including the direction of the shift, size dependence, the absence of significant broadening of the transition linewidth, and the difference between dithiols chain length and hydrazine. One contribution to the total energy of a nanocrystal excited state is the electrostatic polarization of the medium outside the nanocrystal by the free charge carriers excited within the nanocrystal. A larger dielectric constant outside lowers the energy of the nanocrystal excited state via increased electrostatic solvation. For the PbSe QD films considered here, the "solvent" is the matrix of QDs surrounding each individual nanocrystal. As the fraction of organic material (ε= 2.1) within the film decreases due to chemical treatment with either EDT or hydrazine, the average dielectric constant of the film approaches that of PbSe (ε= 23.9), lowering the energy of the nanocrystal excited state. Additionally, as the ligand shell is removed or its thickness is reduced, the distance between high dielectric cores is reduced, increasing the overall effect. Leatherdale and Bawendi showed that the salvation energy for the first exciton in a QD, including the dielectric of the ligand shell, is given by (*32*),

$$\delta = \frac{\pi q^2}{2\varepsilon_1 \varepsilon_0 a} \sum_{l=1}^{\infty} a^{2l+1} A_l \int_0^1 [j_0(\pi x)]^2 x^{2l+2} dx. \qquad (4.1)$$

Where q is the electron charge, a is the radius of the QD core, j_0 is a spherical Bessel function, and the term A_l is given by,

$$A_l = \frac{l+1}{a^{2l+1}} \frac{a^{2l+1}(\varepsilon_2-\varepsilon_3)[\varepsilon_1+l(\varepsilon_1+\varepsilon_2)]+b^{2l+1}(\varepsilon_1-\varepsilon_2)[\varepsilon_3+l(\varepsilon_2+\varepsilon_3)]}{a^{2l+1}(\varepsilon_1-\varepsilon_2)(\varepsilon_2-\varepsilon_3)l(l+1)+b^{2l+1}[\varepsilon_1+l(\varepsilon_1+\varepsilon_2)][\varepsilon_3+l(\varepsilon_2+\varepsilon_3)]}, \qquad (4.2)$$

where b is the distance from the center of the QD to the outside of the ligand shell, and ε_1, ε_2 and ε_3 are the dielectric constants of the QD core, ligand shell and surrounding medium (C/S/M), respectively. This model can also be simplified for the case of hydrazine, by completely removing the shell component ($b = 0$), resulting in a core, medium (C/M) model. The results of the C/M and C/S/M models for each dithiol carbon length are summarized in Figure 4.8. The C/M and C/S/M models have been scaled 20 and 35 times respectively. The theoretical maximum extent of red shift from solvatochromism for differing diameters of PbSe QDs, solvated in a medium of PbSe (C/M model) is shown in Figure 4.11. We see that for a 4 nm QD, the expected shift is only 10 meV, ~10% of the observed shift. From this model, it appears solvatochromism only plays a small role.

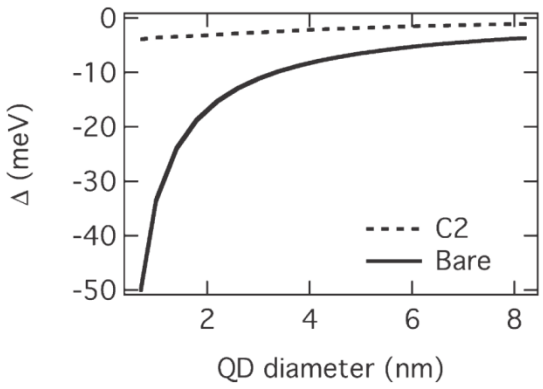

Figure 4.11: Expected red shifts with respect to the OA-capped QDs in the first exciton transition calculated as a function of the diameter of the QD core for C2-capped (dashed) and bare (solid) PbSe QDs in the C/M model.

After eliminating growth, substrate interaction and solvatochromism as sources of the observed red shift, we are left with electronic coupling as the major contributor. There are two ways to understand the increased inter-QD electronic coupling.

The First, is through the electronic exchange coupling energy, $\beta = \langle a|\hat{H}|b\rangle$ (between two neighboring quantum dots a and b). As the inter-particle distance decreases, this would be expected to increase due to more spatial overlap of the wave functions. This would lead to a red shift in the first exciton transition, as illustrated in Figure 5. In particular, for a hexagonally close-packed 2-D assembly of s-orbitals, tight-binding theory predicts that a new electronic band would form If such a band is formed both by the 1s electron and hole levels of the QDs, we can estimate the first exciton transition energy (Δ_E) at a particular inter-particle separation D as

$$\Delta_E = \Delta_E{}^0 - (6|\beta_e| + 6|\beta_h|) \approx \Delta_E{}^0 - 12|\beta|, \qquad (4.3)$$

where $\Delta_E{}^0$ is the first exciton transition energy for isolated QDs, and β_e and β_h are the electron exchange coupling for the electron and hole levels, respectively. Equation (4.3) neglects the exciton binding energy and assumes that β_e and β_h are close in value. This assumption is justified in PbSe due to the similar values for the effective mass of the electron and hole (*96*). For a 3-D QD solid, this model would predict and overall$\Delta_E \approx \Delta_E{}^0 - 24|\beta|$, as there are 12 nearest neighbors in the FCC close packed lattice. For our 2-D assemblies, the $|\beta|$ is as large as 13 meV (4 nm QDs, hydrazine), which is an order of magnitude larger than the same 3-D film. Although large, these values are not unreasonable. A scanning tunneling microscopy and spectroscopy (STM and STS) study of thermally annealed 2-D assemblies of PbSe QDs showed that based on an effective mass model, $|\beta|$ could be as large as 25 meV for an inter-particle separation of 0.5 nm (*51*).

In order to distinguish between the affects of solvatochromism and electronic we investigate the red-shifts in an assembly of two sizes of QDs. By suspending large QDs in a matrix of smaller ones, we will eliminate the electronic coupling component and only observe the effects of salvation inside a QD matrix. The contributions solvatochromism would be $\Delta E^1_{solv.} = \Delta E^1_{mix}$ and the contribution from electronic coupling would then be $\Delta E^1_{coupling} = \Delta E^1_{pure} - \Delta E^1_{mix}$. The results of treating this film with ethanedithiol (C2) are shown in Figure 4.10.

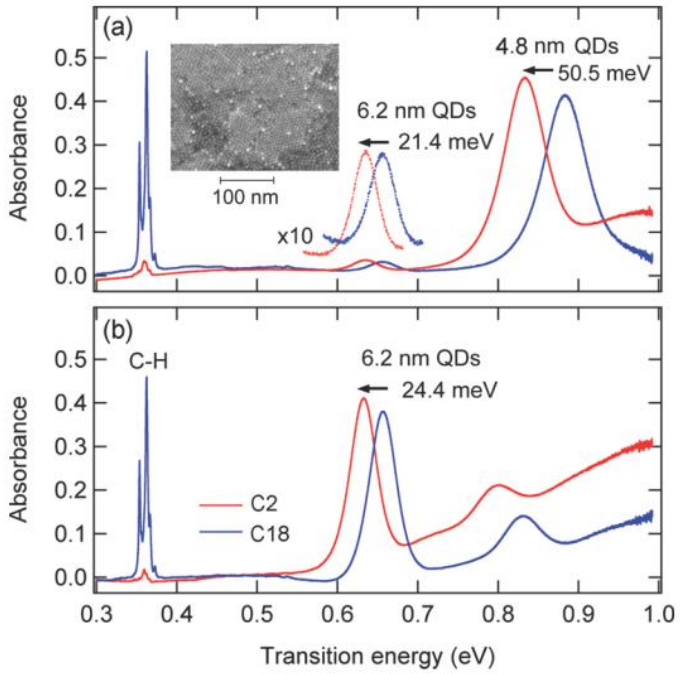

Figure 4.12: (a) Optical absorption spectra for C18- and C2-capped QD films (~2 ML film of large QDs (D = 6.2 nm) embedded in a matrix of smaller ones (D = 4.8 nm) at a number ratio of 1:35. The first exciton peak of the large QDs red shifts by 21.4 meV, while that of the small QDs red shifts by 50.5 meV. The inset shows the SEM image of the mixed QD fi lm; the minority of large QDs (bright spots) are completely isolated in the matrix of small QDs. (b) Optical absorption spectra for a ~2 ML fi lm of large QDs (D = 6.2 nm) before (blue) and after (red) ligand exchange reaction of C18 by C2. The first exciton red shifts by 24.4 meV after the ligand exchange reaction.

In the mixed film (Fig. 4.12) we see that the large QDs (EX^1~0.65 eV) electronically isolated in a matrix of small QDs (EX^1~0.85) have red shift 21.4 meV after exchange with C2. For a film of only large QDs, where electronic coupling is allowed, the red shift is 24.4 meV. This means that 21.4 meV of the shift is due to salvation effects, while only 3.0 meV is due to electronic coupling. The shift due to solvatochromism is much larger than the C/S/M would predict possible.

How is there such a disparity between the model and experimental results? We propose the answer lies in the sensitivity of the polarization stabilization energy to the spatial distribution of the electron or hole wave function. For a point charge located from an interface between two phases with different dielectric constants, the polarization energy (charge image interaction energy) scales inversely with distance to the interface; for a planar interface, the scaling factor is (4z)-1 (z is distance to the interface) (*97*). The sensitivity of the polarization energy is also reflected in the calculated Δ as a function of QD size, Figure 4.9. For the same capping molecule shell thickness (or bare QDs with no molecular shell), the magnitude of the calculated first exciton red shift increases nearly exponentially with decreasing QD size. As the QD becomes smaller, the spatial distribution of the electron (hole) wave function lies closer to the interface with the dielectric medium, leading to a larger polarization effect.

There are multiple reasons that the distribution of the electron and hole may deviate from the spherical well model. The first is that the actual boundary condition is not a step-like potential profile, as used in the model. This idea is invoked when understanding carrier dynamics in QD solids (*98*). The second cause may be the perturbation approach in deriving equation 4.1 and 4.2. For example, the red shift reaches almost 10% of the optical band gap for PbSe with hydrazine treatment, suggesting a perturbation treatment may be inadequate. The third cause may result from deviation of

the QD shape from the spherical model, leading to partial localization of the electron (hole) wave function to one part of the QD, as seen previously in scanning tunneling spectroscopy measurements (*99*). All of these factors can lead to much larger polarization effects than what are predicted from the spherical quantum well approximation.

Chapter 5: Electron Transfer from Quantum Dots: Two Domains

Portions of this chapter have been published as:

> W.A. Tisdale, K.J. Williams, B.A. Timp, D.J. Norris, E.S. Aydil, and X.-Y. Zhu, "Hot-Electron Transfer from Semiconductor Nanocrystals", *Science* **328**, 1543 (2010)

Much of the content of this chapter has been submitted as:

> K. J. Williams, C. A. Nelson, A. Jailaubekov, L. G. Kaake, X.-Y. Zhu, "Resonant state mediated electron transfer from CdSe Quantum Dots to Single Crystal TiO_2" *Submitted to J. Phys. Chem. Lett. (2012)*

In this chapter, we detail the dynamics of electron transfer from lead selenide (PbSe) and cadmium selenide (CdSe) quantum dots (QDs) to the (110) face of single crystal rutile titanium dioxide. Electron transfer at the interface between QDs and bulk semiconductors is a key step in QD based optoelectronics. We probe electron transfer using the surface and interface sensitive technique of time resolved second harmonic generation. For the case of PbSe QDs we report unltrafast electron transfer from hot (above conduction band minimum "CBM") states to a titanium dioxide. Contrary to PbSe QDs, CdSe QDs do not undergo hot electron transfer, and exhibit slower transfer rates when pumped at energies above the conduction band minimum.

5.1 INTRODUCTION

Colloidal semiconducting quantum dots (QDs) are of interest as light absorbing material for next generation solar cells because of their advantages of high absorption coefficient, tunable band gap, and solution processability (*2,100*). The most popular approach is the QD sensitized solar cell (QDSSC) (*10,101*) which uses QDs to replace organic dye molecules in the more traditional Grätzel Cell (*5*). In a QDSSC, QDs are

adsorbed on a wide bandgap semiconductor (e.g. TiO_2) to serve as the photoanode (*102*). In order to obtain a large interfacial area and sufficient light absorption, a highly porous film of wide gap semiconductor nanoparticles is often used as the electron acceptor. While this approach is necessary from a device perspective and advantageous in terms of signal level in absorption spectroscopies, the highly disordered and heterogeneous nature of nanoporous films makes characterizing and controlling the important donor-acceptor interface difficult. Here we use the model system of either lead selenide (PbSe) or cadmium selenide (CdSe) QDs adsorbed on the (110) face of atomically flat, single crystal, rutile TiO_2 to provide a well controlled and characterized donor/acceptor interface. To compensate for the much-lower interface area than that of nanoporous TiO_2 thin films, we apply the highly interface specific technique of time resolved second harmonic generation (TR-SHG) (*24,103*). The use of TR-SHG on single crystal TiO_2 allows us to track the signatures of electron transfer and their dynamics from hot and cooled electronic states.

By examining both PbSe and CdSe quantum dots we can compare the role of Bohr radius and energetic alignment in electron transfer, in otherwise similar materials. For the case of PbSe QDs (large Bohr radius, below CBM alignment) we observe ballistic transfer from thermally “hot" electrons, followed by drift of the ballistically injected electron in TiO_2. For CdSe (small Bohr radius, at/above CBM alignment), electron transfer rates slow as QDs are pumped above their lowest energy “cooled” state. The electrons do not drift in TiO_2, suggesting a mechanism of electron transfer mediated by localized surface states near the TiO_2 conduction band.

5.2 EXPERIMENTAL DETAILS

The following section details the experimentation carried out on the CdSe QDs. For further details on the PbSe QD synthesis and sample preparation details of that system please refer to chapter 4.

Cadmium selenide nanocrystals were synthesized using a method by Reiss et al (*104*). In brief, cadmium oxide (51.3 g), trioctylphosphine oxide (1.012 g), hexadecylamine (2.317 g) and tetradecylphosphonic acid (222 mg) were added to a three neck flask. Precursors were heated to 100 degrees Celsius under vacuum and purged two times with nitrogen. The solution was heated to 270 °C until the solution was clear and then cooled to 250 °C. Nucleation was started by quickly injecting 2.5 mL of selenium shot dissolved in trioctylphosphine (0.2 M). The reaction was monitored with UV-Vis (Ocean Optics USB4000) and quenched with toluene when nanocrystals had reached the desired size. Precipitations were carried out with 1 part quantum dot solution to 1 part methanol. The solution was then centrifuged at 2,500 RPM for 5 minutes, the supernatant was discarded and the quantum dots were redispersed in toluene. Precipitations were repeated 5 times to remove excess ligands. The synthesis was monitored by visible absorption.

The QD samples were characterized by absorption spectroscopy (OceanOptics USB4000) and fluorescence spectroscopy (Horiba Fluorolog-3 at an excitation wavelength of 485 nm). Figure 1d shows absorption and fluorescence emission spectra for the QDs used in this work. The first exciton peak is at 2.00±0.02 eV in absorption and 1.92 ± 0.01 eV in emission. The first exciton peak position corresponds to a QD diameter of 5 nm (*105*). For this QD size, previous ultraviolet photoelectron spectroscopy (UPS) measurements measure the $1S_e$ level of the QD to be near the conduction band minimum of TiO_2 (*106,107*).

Atomic force microscopy images were collected in Tapping mode using an Asylum Research MFP-3D AFM, with a 50 kHz 5 N/m cantilever (AppNano).

Ultraviolet photoelectron spectroscopy (UPS) was used to determine interfacial alignment of occupied energy levels (see next section). All UPS spectra were collected at room temperature on the same instrument used for XPS. He-I radiation ($h\nu$ = 21.2 eV) was used as the UV light source, and the lamp power was set at 25 W. Incident light was 50˚ from the surface normal, and photoelectrons were collected along the sample surface normal direction with an analyzer pass energy of 4.45 eV and a sample bias of -8.0 V

Single Crystal rutile cut 1x1 cm along the (110) face were purchased from MTI corp. Crystals were rinsed with toluene, sonicated for 30 minutes in acetone, rinsed with deionized water and submerged for 30 minutes in a 10 mmol solution of sodium perchlorate under UV illumination (*108*). Crystals were immediately rinsed with deinonized water, then acetonitrile and submerged in a 1:10 solution of 3-mercaptopropionic acid (MPA) in acetonitrile for 24 hrs. Once removed from the MPA solution, crystals were immediately rinsed with toluene and placed in a 10 mg/mL solution of CdSe quantum dots in toluene for 4 hrs. The QD sensitized TiO2 crystals were removed from the solution, rinsed thoroughly with Toluene to remove weakly adsorbed QDs and immediately mounted in an optical vacuum chamber (Janis ST-100).

TR-SHG measurement were carried out using a seeded Ti:sapphire regenerative amplifier (Coherent RegA9050) with a 250 KHz repetition rate and a pulse duration of 70 fs. The laser beam was split into two paths. The first beam could be passed through an optical parametric amplifier (Coherent OPA) to generate pump laser light at 570-635 nm or 950-1600 nm or could bypass the OPA and remain at the fundamental wavelength (820 nm). The pump beam was focused onto the sample surface to give a pulse energy density of 80 μJ/cm2, which corresponds roughly to the excitation of one electron hole

pair per QD per laser pulse (η=1). The second laser beam was directly used as probe (820 nm) and focused on the surface to give a pulse energy density of 20 μJ/cm2. The reflected probe beam was passed through color filters and a monochromator (Oriel Cornerstone 130 1/8M) and the residual second harmonic signal at 410 nm was detected by a photomultiplier tube (Hamamatsu R4220P). A full optical layout can be seen in section 3.4 of chapter 3. Figure. 1 illustrates the orientation of the crystal with respect to the probe beam (left) and resulting electric field (right).

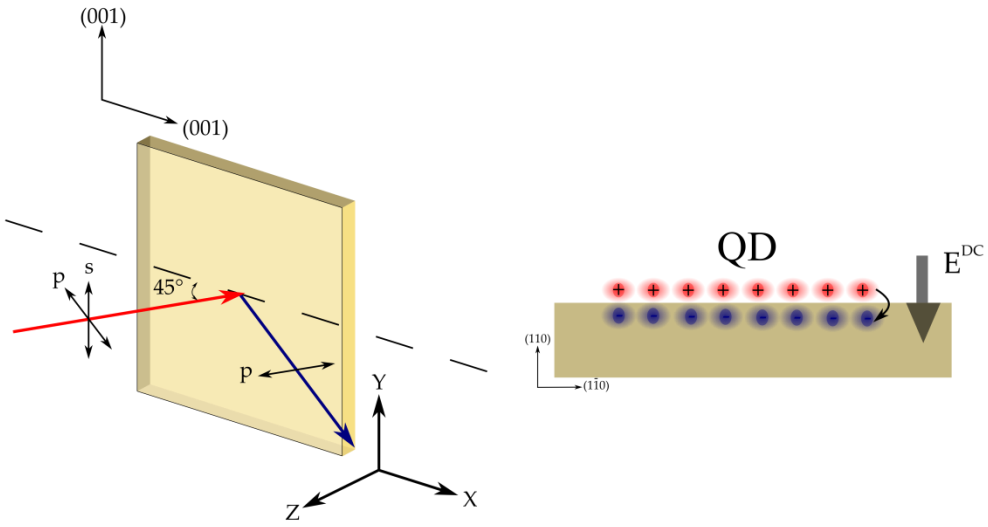

Figure 5.1: Left: illustration of the crystal orientation and optical polarization used for SHG in reflection from the rutile (110) surface, the optical plane is perpendicular to the (001) plane. Right: illustration of the transient electric field created when electron transfer occurs from solid state QDs.

5.3 PbSe QDs: the Delocalized Electron Transfer

PbSe has an extremely large exciton Bohr radius (46 nm) such that charge carriers in sub-10-nm diameter PbSe quantum dots are subject to strong quantum confinement effects (*96*), and their electronic wave functions will extend spatially well beyond the nanocrystal surface. This delocalization facilitates electron transfer if the nanocrystals are

close to an electron accepting substrate. We chose rutile TiO_2 for this role because it not only is technologically relevant and available as a single crystal, but it also has a very large density of accepting states.

5.3.1 Sample Characterization

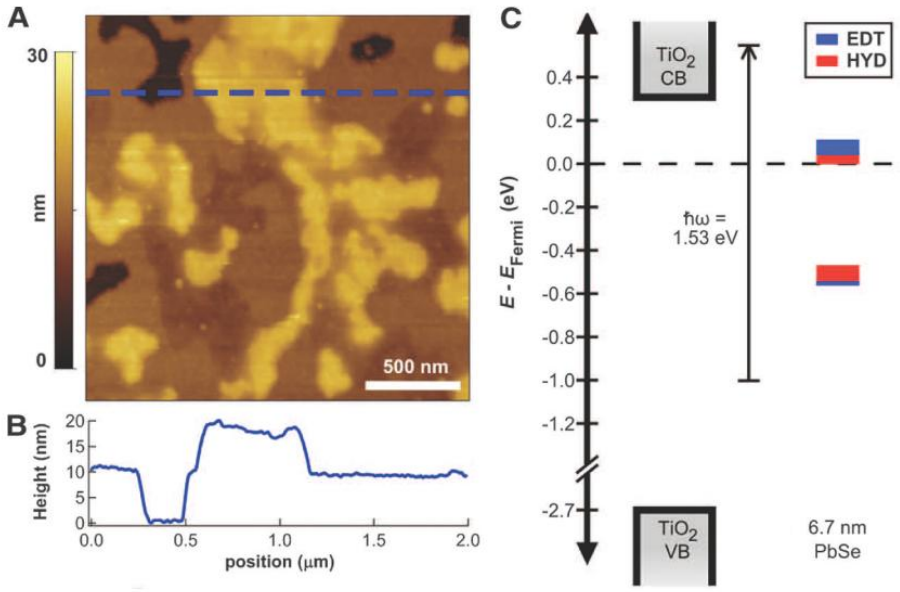

Figure 5.2: (A) Atomic force micrograph showing the morphology of a ~1.5 monolayer film of 6.7 nm oleic acid-capped PbSe nanocrystals supported on atomically flat TiO_2. (B) Line height profile corresponding to the dashed blue line in (A). (C) Alignment of highest occupied and lowest unoccupied quantum dot energy levels relative to the TiO_2 conduction band edge following chemical treatment of the nanocrystal surface. VB = valence band; CB = conduction band; EDT = 1,2-ethanedithiol; HYD = hydrazine.

Figure 5.2 shows the AFM and UPS results from the PbSe nanocrystals (6.7 nm). The AFM data shows that the QD coverage was ~1.5 monolayer. A single line trace indicates a step height of ~11 nm for the QD film, which is consistent with a 6.7 nm with a 2 nm thick ligand shell on both sides. As with all strongly confined semiconductor nanocrystals, the energy of excited electron states in PbSe quantum dots increases with

decreasing particle size. Thus, we first used ultraviolet photoelectron spectroscopy (UPS), in conjunction with optical absorption, to determine the energy of the lowest excited electronic state in our nanocrystals. We found that, regardless of particle size or chemical treatment, this state was always below the TiO_2 conduction band minimum (Fig. 1C). As a result, electron transfer from PbSe to the TiO_2 conduction band should only be possible from hot electronic states of the quantum dot (*60*).

5.4.2 TR-SHG Dynamics of PbSe QDs on TiO_2

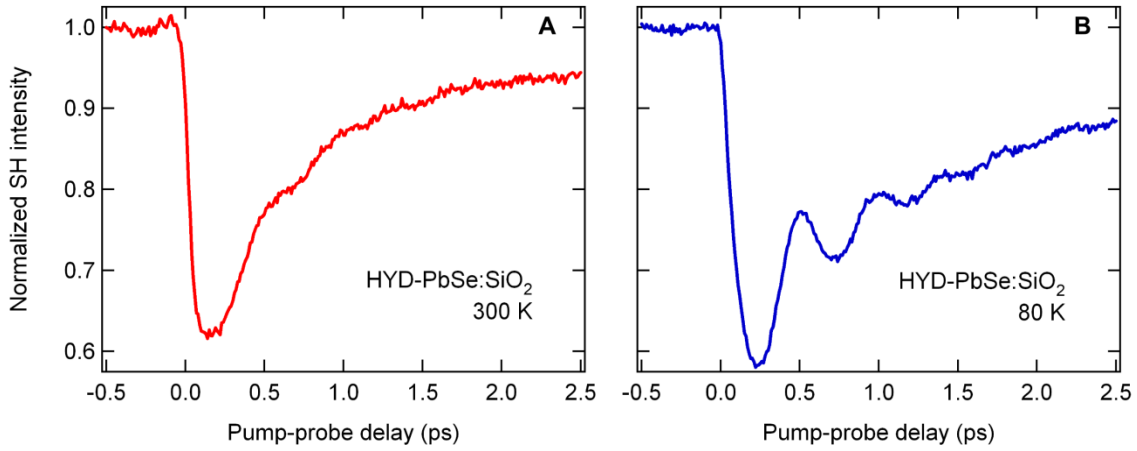

Figure 5.3: TR-SH response of hydrazine (HYD)-treated PbSe nanocrystals (d = 6.7 nm) on SiO_2 at (**A**) 300 K and (**B**) 80 K. The SH signal recovers faster at 300 K (~0.5 ps time constant) than at 80 K (~3 ps time constant). Coherent phonon oscillations are more evident at lower temperatures due to slower dephasing.

As a control, films of QDs were made on amorphous silica. This control should allow us to observe a system free from electron transfer, and should not include positive changes in SH instensity caused by the electric field induced second harmonic (EFISH) mechanism. Indeed, we measure a drop in SHG intensity upon photoexcitation of our PbSe films supported on amorphous silica glass (at all quantum dot sizes, treatments, and

temperatures). Because glass has a bandgap too wide to accept electron transfer from our quantum dots, we attribute this reduced intensity to their intrinsic SHG response (Fig. 5.3). It is also worth noting that although the signal recovery rates are in relative agreement with electron cooling rates in PbSe, it is difficult to assign which states the electrons may be cooling from based only on second harmonic generation intensities.

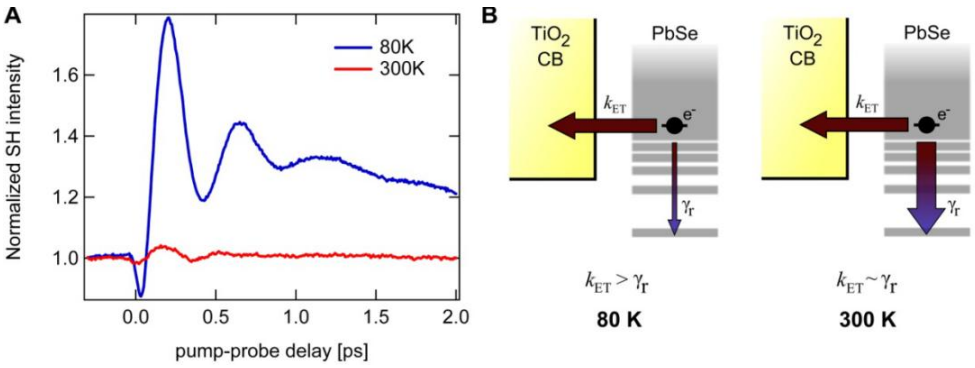

Figure 5.4: (A) Time-resolved second harmonic response of the TiO_2 surface coated with 1.5 monolayers of hydrazine-treated 3.3 nm PbSe nanocrystals. The large rise in SHG intensity is indicative of efficient electron transfer from PbSe to TiO_2. (B) Illustration of the competing pathways of interfacial electron transfer and intra-quantum-dot relaxation. At higher temperatures, hot electron relaxation (γ_r) becomes competitive with interfacial electron transfer (k_{ET}).

In contrast to the drop in amorphous silica films, we observe a significant rise in SHG intensity after photoexcitation of the quantum dots on TiO_2 at 80 K (Fig. 5.4A). This response is consistent with efficient hot electron transfer from PbSe to TiO_2 for several reasons. First, the SHG signal rises on a timescale shorter than the laser pulse (50 fs). Such an ultrafast response would be expected for the strong-coupling limit of electron transfer. Also, because the electronic relaxation time between the first two excited states in similar-sized PbSe quantum dots has been measured as 540 fs at 300 K (*109*), electron

transfer must be significantly faster, outpacing the cooling process. Second, the magnitude of the ultrafast SHG response decreases with increasing temperature (Fig. 5.4A). As the PbSe quantum dots are warmed to 300 K, the time constant for electron transfer should be largely unaffected in the strong-coupling limit. However, the electronic relaxation rate is known to increase exponentially (*109*). Thus, at higher temperatures cooling of hot electrons can compete with hot electron transfer (Fig. 5.4B). Thermally relaxed electrons cannot transfer to TiO_2 from PbSe QDs, therefore, accelerated cooling leads to a decrease in SHG signal. As a negative control, we observe no electron transfer when we decrease the pump photon energy to below the threshold necessary to reach the conduction band minimum of TiO_2 (Fig. 5.5).

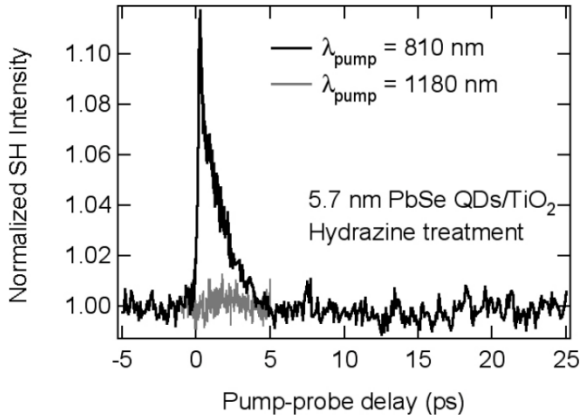

Figure 5.5: SHG response of PbSe nanocrystals (d = 5.7 nm) on TiO_2 (treated with hydrazine) at 80 K for two different pump laser wavelengths: λ pump = 810 nm (black) and λ pump = 1180 nm (grey). The laser power at each wavelength was chosen to maintain an average excitation of 1.0 electron-hole pairs per nanocrystal.

These results indicate hot electron transfer from semiconductor nanocrystals to a technologically relevant electron acceptor is possible. This effect is expected to be of general significance to other semiconductor nanocrystals and electron/hole conductors,

provided the hot electrons and holes possess sufficiently long lifetimes and the interfaces are properly controlled to enable ultrafast charge transfer. Moreover, if hot electron (hole) transfer can be controlled to occur in very narrow energy windows to also minimize loss in the electron (hole) conductor, the highly efficient hot carrier solar cell may be realized.

5.4 CdSe QDs: the Localized Electron Transfer

CdSe has a much smaller Bohr radius (5 nm) than PbSe, and therefore the exciton wavefunction will not extend far beyond the nanocrystal surface, potentially limiting its coupling with the bulk conduction band of TiO_2. Ultrafast electron transfer is limited to states that can couple strongly to the CdSe QDs.

5.4.1 Sample Characterization

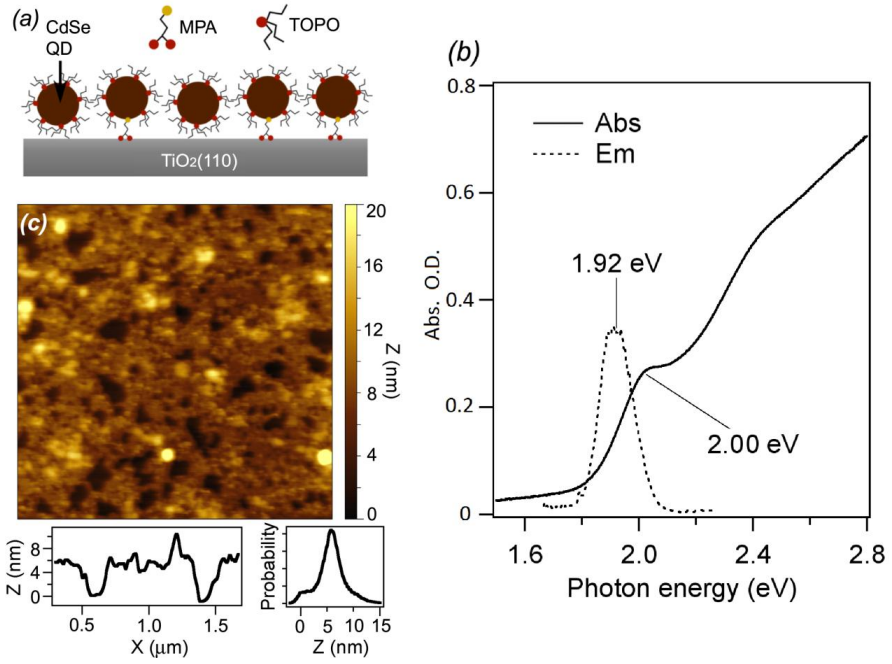

Figure 5.6: (a) Illustraion of TOPO capped CdSe QDs anchored to the TiO_2 crystal via MPA (b) Absorbance and emission spectra of 5nm CdSe QDs. (c) 2μmx2μm AFM false color image with single line scan and height histogram.

The sample preparation procedure described in Section 5.2 should lead to near monolayer coverage of isolated QDs capped with mostly TOPO ligands, with only some MPA ligands between each QD and the TiO_2 surface replaced by surface bound MPA molecules, as illustrated in Figure 5.6a. Although it is possible to exchange the majority of TOPO ligands with MPA in a solution treatment, this would result in aggregation of the QDs on the surface. Figure 1c shows an AFM image (2 μm x 2 μm) of a TiO_2 surface with an adsorbed QD coverage of approximately one monolayer. Most of the surface area is covered with a QD monolayer of 6 ± 1 nm apparent height, with some bare spots (dark) and a few bright islands of a second layer as clearly shown in a cross sectional profile below the image. Also shown is a height histogram which gives an average height of ≥ 6 nm, as expected from the diameter of the QD plus the TOPO ligand shell. A solution absorbance spectra is shown in Figure 5.6b from a 1:20 toluene dilution of the solution of ~10mmol QD solution used to prepare films; in a 1 cm quartz cuvette.

5.4.2 TR-SHG Dynamics of CdSe QDs on TiO_2

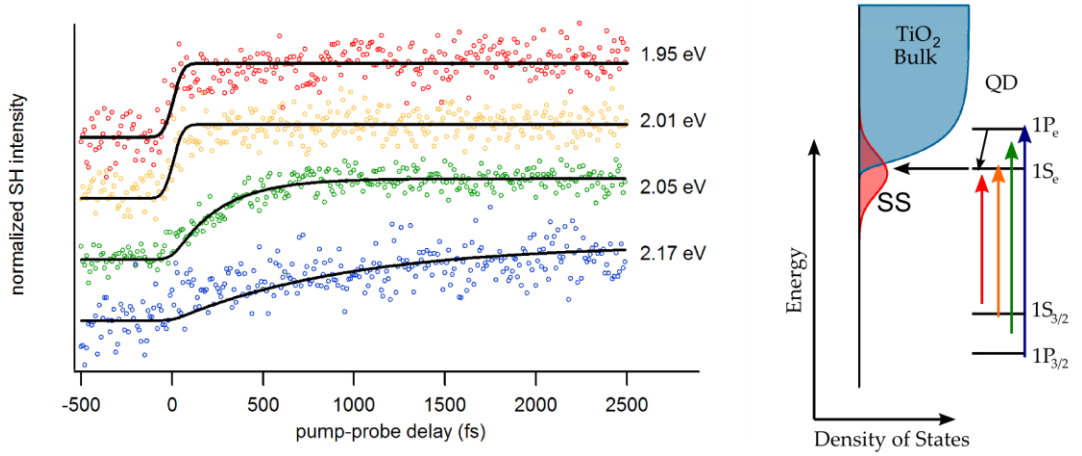

Figure 5.7: Left: Pump-induced SHG signal as a function of delay time for four pump hν (blue: 2.17 eV; green: 2.05 eV; brown: 2.01 eV; and red: 1.95 eV). The black dashed curves are fits to rate equations. The spectra are offset vertically for clarity. Right: illustration of photo-induced resonant electron transfer from the $1S_e$ level in QDs to the TiO_2 surface states. Direct coupling between higher-lying electron states in QDs and the TiO_2 conduction band is weak.

Figure 5.7 shows TR-SHG measures for the monolayer CdSe QD/TiO_2 sample at the indicated pump laser wavelengths. We normalized each spectrum to the static SHG intensity (at negative time delays) and then subtract the static intensity to show only pump-induced changes (ΔI_{SHG}). The spectra are offset for clarity. At every pump photon energy, we see a rise in SHG signal due to photo-induced electron transfer from CdSe QDs to TiO_2 and the establishment of an interfacial electric field. (*24*,103). The rate of electron transfer clearly depends on photon energy. Quantitative analysis was carried out by fitting each time-dependent SHG profile to a convolution of a single exponential with a cross-correlation of pump and probe pulses. The fits are shown as dashed curves. At

the lowest pump photon energies (1.95 & 2.01 eV) which are resonant with the first exciton transition in absorption spectrum, we find the time constants for charge transfer to be ultrafast, below the time resolution of our measurement (~30 fs). As the excitation photon energy is increased above the first exciton transition, τ_{CT} slows to 250 ± 20 fs at $h\nu$ = 2.05 eV and 1.0 ± 0.1 ps at $h\nu$ = 2.17 eV.

The inverse relationship between the electron transfer rate and the excitation photon energy is unexpected. As the incident photon energy is increased, there is a concomitant increase in the energy of the excited electron in CdSe which leads to more energetic driving force (i.e., electron energy above the TiO_2 conduction minimum) as well as a higher density of acceptor states in TiO_2. For a traditional dye sensitized solar, where photo-induced electron transfer occurs from a localized molecule to the delocalized conduction band of a metal oxide, one expects increased electron transfer rate with increasing electron energy (*61*,*110*). This is clearly not the case for hot electrons in CdSe QDs. Thus, we believe that the nascent hot electron from the initial photo-excitation is not strongly coupled to the TiO_2 substrate. Rather, the hot electron must first relax to the $1S_e$ level, before efficient transfer to the TiO_2 substrate. Supporting this interpretation, we find that the electron transfer time constants of 250 fs and 1 ps at $h\nu$ = 2.05 eV and 2.17 eV, respectively, are comparable to the hot exciton cooling rate from the p-like ($1P_{3/2}$ $1P_e$) to the s-like ($1S_{3/2}$1Se) states (*10*). Solution studies of CdSe QDs by transient absorption (TA) have measured the cooling rate for electrons from the $1P_e$-$1S_e$ for QDs of the size used in this study to be 250 fs (*111*). While making quantitative comparisons between a QD solid film linked to an acceptor and a well passivated solution is difficult, considering

competition from surface trapping of hot electrons or those surface states as a path to charge separation, the observed slowing of the transfer rates is in relative agreement (*111)*. The cooling rate for electrons from the $1P_e$-$1S_e$ is an order of magnitude slower than the transfer observed at lower energies (<30 fs), suggesting that competition from electron cooling alone may not be enough to explain why the electron first cools before transferring.

Why might electron transfer occur much more efficiently for lower energy electrons at the $1S_e$ level, near the CBM of TiO_2? It is known that a high density of surface states exists near the CBM of TiO_2 (*107,112*). These surface states may play important roles in charge separation and recombination in sensitized TiO_2 solar cells (*113*). It is not surprising that the CdSe QD can interact strongly with these local surface states when the electronic state in the QD (i.e., $1S_e$) is in resonance. In the present case, the QDs capped with bulky TOPO ligands are only linked to the TiO_2 surface through a few surface bound MPA molecules. These capping molecules prevent the direct electronic interaction between electronic states in CdSe QDs to the conduction band states of TiO_2. In contrast, PbSe has a much larger Bohr radius than CdSe and the enhanced quantum confinement effect leads to a greater extension of the electron wavefunction beyond the physical boundary of the PbSe QDs. This effect, when coupled with the removal of long chain capping molecules or the replacement by smaller ones, leads to direct electronic coupling between hot electron states and the TiO_2 conduction band. As a result, hot electron transfer and subsequent recombination occurs readily from PbSe QDs to TiO_2 (*24*). Whereas CdSe QDs linked to a single crystal TiO_2 surface via MPA linkers, the more

localized coupling between QD $1S_e$ level to TiO_2 surface states may essentially give rise to a resonant channel for efficient electron transfer. For hot electrons with energy off resonance, cooling to the $1S_e$ level is necessary before efficient electron transfer can occur. This resonant mechanism is summarized in Fig. 3. One may imagine taking advantage of such an interface-mediated mechanism to engineer resonant channels for controlled electron transfer. Note that in sintered TiO_2 films, one expects a higher density of defect surface states over a broader energy range (*111*). This may allow for efficient charge transfer from hot electron states in QDs.

Chapter 6: Following the Path of Hot Electrons

6.1 INTRODUCTION

Graphene, consisting on a single atomic layer of graphite, has generated considerable excitement for its unique physical properties. A bulk sheet of graphene has a 0 eV bandgap and incredibly high extinction coefficient, allowing an atomic layer sheet to absorb 2.3% of incident light (*35*). Additionally the linear dispersion relationship near the Fermi level allows for very efficient electron-electron scattering, and low electron-phonon scattering, an ideal property for a hot carrier solar cell material (*22*). By controlling the size of the graphene sheet, electronic and optical properties, such as the bandgap, can be tuned.

One major challenge when working with graphenes is their propensity for sticking together, making graphitic structures. By forming graphitic structures, the optical properties and electrical properties change, while also making them difficult to solubilize. Recently, the synthesis of large, solution processable, graphenes with solubilizing side alkyl groups has been developed, leading to the realization of colloidal graphene quantum dots (QDs) (*23*).

Colloidal graphene QDs are a quantum-confined system that could serve as light absorbers in photovoltaic devices (*23,33*). Made synthetically from organic chemistry routes from small organic molecules, they have properties resembling more nanocrystalline solids than molecules. For example, graphene QDs have continuous absorption spectra in the UV-visible region due to the overlap of electronic absorption bands caused by closely spaced electronic energy levels and vibronic coupling. (*23,34*). The graphene QDs have also been shown to have slow hot-carrier cooling dynamics (*36*), reminiscent of the "phonon bottleneck" which has been intensively investigated in conventional semiconductor quantum dots. (*37*).

Because grapheme QDs are made of the most abundant elements on earth and contain no rare or toxic metals, graphene QDs are attractive for various energy-related applications. With extinction coefficients as high as $1x10^5$ M^{-1} cm^{-1} in the visible range,16 they make better light absorbers than extensively studied ruthenium complexes. Their band gap is tunable, in principle, to as small as 0 eV. Graphene QDs have interesting potential as a material for next generation solar cells due to their extraordinarily long lifetimes of hot carriers (*36*), potentially allowing for hot-carrier transfer or multi-exciton generation that could overcome the Shockley-Queisser limit in solar energy efficiency (*22,100,114*)

6.2 EXPERIMENTAL DESIGN

The following section details the experimentation carried out on graphen QDs. Some of the TR-SHG data discussed briefly in this chapter was performed using PbSe QDs. For further details on the sample preparation, TiO_2 cleaning procedures and TR-SHG measurement details of that system please refer to chapters 4 and 5 respectively.

6.2.1 Sample Preparation

The graphene QDs used in this study consist of a 132 carbon, graphene core, solubilized by two 2,4,6-trialkyl-substituted phenyl groups and functionalized with a carboxylic acid group and will be referred to as C132A (Figure 6.1b). C132A QDs were received from Li and colleagues at the University of Indiana, and were synthesized by standard procedures (*115*). After being dispersed in a minimal amount of chloroform in a scintillation vial, a rutile (110) single crystal (MTI corp) was submerged in the solution, the vial was capped, and the chloroform was allowed to slowly evaporate in excess of 24 hr. Enough chloroform was added to the vial to redissolve the excess C132A and was again capped and left to dissolve for an excess of 24 hr. Chloroform was again used to

re-dissolve excess C132A and the rutile crystal was removed, lightly rinsed with chloroform and dried under a stream of nitrogen.

6.2.2 SAMPLE CHARACTERIZATION

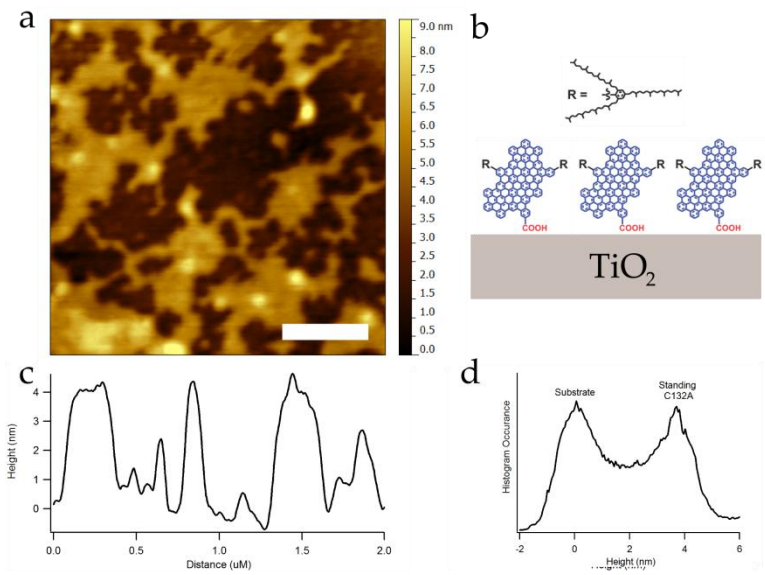

Figure 6.1: (a) 2 µm x 2 µm AC-AFM image of C132A QDs on TiO_2, white scale bar is 500 nm. (b) Illustration of C132A QDs standing on TiO_2 crystal, R is a solubilizing 2,4,6-trialkyl-substituted phenyl group. (c) Single line height trace from **a**. (d) Histogram of heights from **a**.

Surface coverage and molecular orientation were investigated using alternative contact atomic force microscopy (AC-AFM). Atomic force microscopy was carried out on an Asylum Research AFM (MFP-3D) scanning in closed loop. A silicon tip integrated with a rectangular, uncoated silicon cantilever (Applied Nanostructures, < 10 nm radius of curvature, 3 N/m nominal spring constant, resonance frequency of ≈70 kHz, and quality factor of ~140) was used in AC mode.

A 2 µm x 2 µm AC-AFM image reveals tightly packed domains of the C132A QDs on the TiO_2 surface (Fig. 6.1a). A single line trace from the AFM image (Fig. 6.1c)

and histogram of the height at every pixel of the image (Fig. 6.1d) show that the average height of the domains is ~4 nm, which corresponds to the C132A molecules adopting the anticipated on-end or standing conformation (*116*). Figure 6.1b shows an illustration of the C132A QDs standing on the TiO_2 surface. Yan and co-workers propose that the C132A stands on polar surfaces and metal oxides because of the interaction with the acid group. It is well known that carboxylates can form bidentate linkages on TiO_2 and other metal oxides (*117*). C132A QDs, standing in a monolayer, can pack with densities as high as one QD per 2 nm^2 (*116*). By integrating the histogram data in Figure 6.2d, the surface coverage was determined to be ~50%.

The crystal was then oriented in a controllable atmosphere vacuum chamber, capable of heating and cooling (Janis ST-100, Cryostat; Lakeshore, Temperature Controller), for subsequent TR-SHG measurements.

6.2.2 TR-SHG details

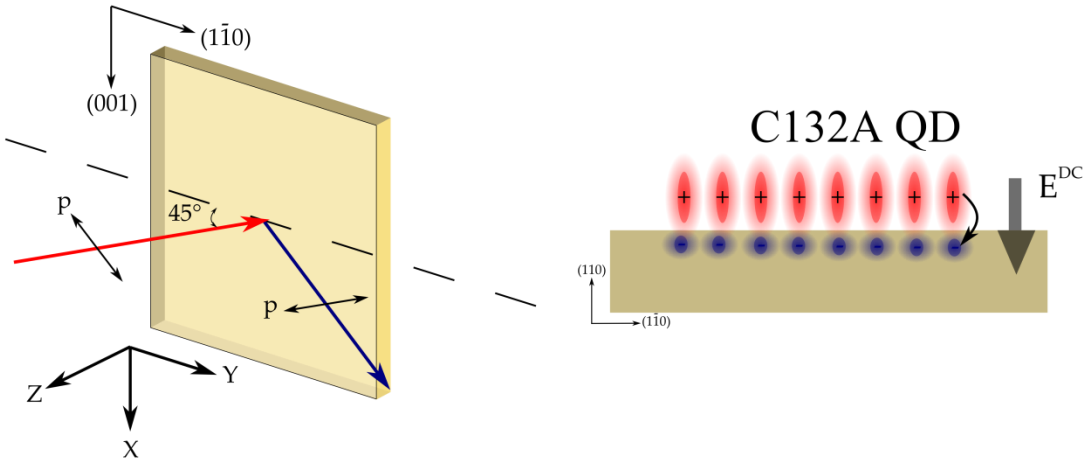

Figure 6.2: Left: illustration of the crystal orientation and optical polarization used for SHG in reflection from the rutile (110) surface, the optical plane is parallel to the (001) plane. Right: illustration of the transient electric field created when electron transfer occurs from C132A QDs.

The Rutile (110) crystal was mounted in the cryostat with the (001) facing downward as is illustrated in Fig. 6.2. When samples TR-SHG measurements were collected at room temperature, the cryostat was kept under positive static pressure with nitrogen, to avoid photo-oxidation. Previous to cooling the sample, the cryostat was evacuated to high vacuum using a turbo-pump (10^{-7} torr). Laser fluence was controlled to provide excitation densities of the C132A of $\eta = 0.5$, calculated using a molar absorptivity at 520 nm of $\epsilon = 1x10^5\ M^{-1}cm^{-1}$.

The two pump energies used for the TR-SHG measurements were 2.0 eV and 2.4 eV, which correspond to wavelengths of 620 nm and 515 nm respectively. Energies between 2.1-2.3 eV were avoided, degenerate four-wave mixing results in the generation

of photons at frequencies unresolveable from the SH frequency being measured (for more details refer to section 3.4).

6.3 TR-SHG DYNAMICS OF HOT ELECTRONS IN GRAPHENE QDS

It has been shown in the previous chapter that nanocrystal QD sensitizers on TiO_2 undergo at least two different regimes of ultrafast electron transfer. Sensitizer which can strongly couple to the conduction band at energies above the conduction band minimum (PbSe QDs) may undergo ballistic electron transfer from "hot" states above the conduction band minimum (CBM) (*24*), while sensitizers that do not strongly couple to the TiO_2 conduction band above the CBM (Large CdSe QDs) have ultrafast transfer, but only to localized states near the interface at energies near the CBM of TiO_2.

Transient absorption studies have shown that dye molecules adsorbed to TiO_2 through a carboxylate mediated bidentate linkage undergo ultrafast electron injection (*61,110*). Graphene QDs have properties of both a small molecule and a semiconducting nanocrystal, and could therefore directly adsorb to TiO_2 and inject electron from states that have not thermally relaxed.

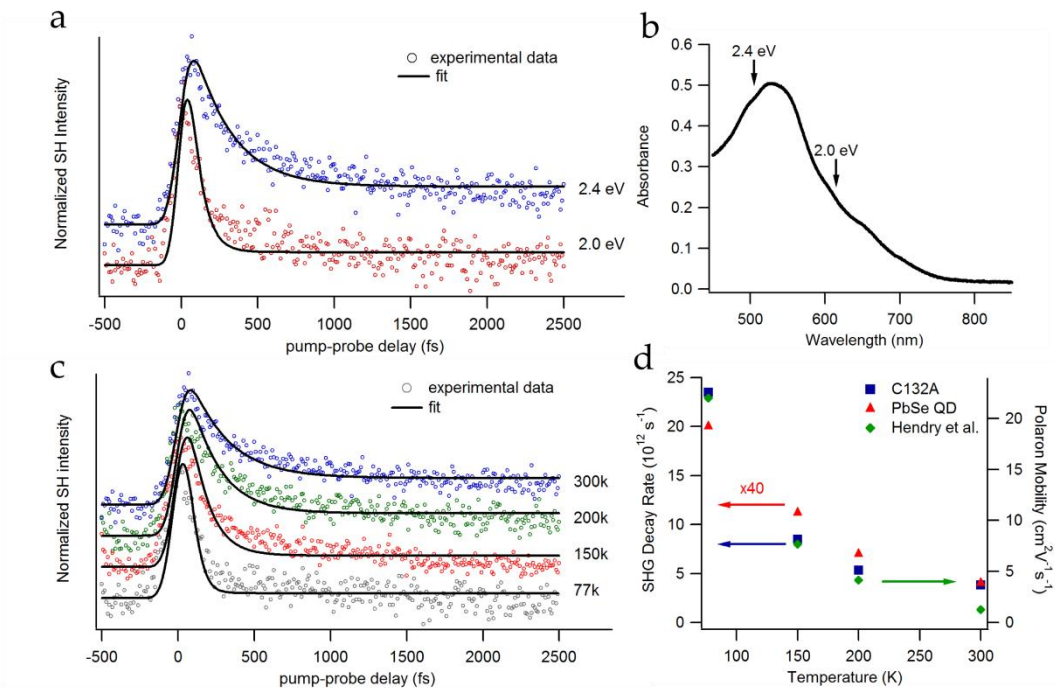

Figure 6.3: (a) Time resolved SHG data from C132A sensitized TiO_2 at 300K and pump energies of 2.0 eV (red circles) and 2.4 eV (blue circles), fit to a pulse width convolved exponential decay (black solid curve). Plots have been normalized and offset for clarity. (b) Absorbance spectra of C132A in chroloform, arrows mark the two pump energies used in **a** (c) Time resolved SHG data from C132A sensitized TiO_2 pumped at 2.4 eV at various temperatures: 300K (blue circles), 200K (green circles), 150K (red circles) and 77K (grey circles). Plots have been normalized and offset for clarity. (d) SHG recovery rate plotted against temperature for C132A (blue squares, left axis) and PbSe QD (red triangles, left axis) sensitized TiO_2 (*24*), plotted with the mobility of polarons in TiO_2 moving perpendicular to the c-axis (green diamonds, right axis) (*118*). PbSe decay rates have been scaled x40.

The results of TR-SHG measurements of end-on aligned C132A sensitized TiO_2 are shown in Fig. 6.3. The results of pumping a C132A monolayer, held at 300K, at 2.0 eV and 2.4 eV (Fig. 6.3b) can be seen in Fig. 6.3a. At both energies, the SH intensity immediately increases at $t = 0$ pump-probe delay, faster than the time resolution of the instrument (<30fs). By convolving an instantaneous rise and exponential decay with the

instrument response function (Gaussian pulse; $FWHM^{2.0\ eV} = 65$ fs; $FWHM^{2.4\ eV} = 80$ fs), the data was fit and the lifetimes of the transient ΔI^{SHG} were $\tau^{2.0\ eV} = 92 \pm 5$ fs and $\tau^{2.4\ eV} = 263 \pm 12$ fs. Reported uncertainties are one standard deviation from the fit.

The temperature dependant SH recovery dynamics were measured at a pump energy of 2.4 eV at temperatures of: 300K, 200K, 150K and 77K (Fig. 6.3c). The data was fit as described above, the lifetimes of the ΔI^{SHG} at each temperature were: $\tau^{300\ K} = 263 \pm 12$ fs, $\tau^{200\ K} = 187 \pm 12$ fs, $\tau^{150\ K} = 117 \pm 7$ fs and $\tau^{77\ K} = 42 \pm 4$ fs. When the C132A QD ΔI^{SHG} decay rates are plotted with PbSe QD ΔI^{SHG} decay rates measured by Tisdale et al. (Fig. 6.3d) (*24*), we see that although the C132A signal decays approximately 40 times faster, both materials have a temperature dependence that is proportional to polaron mobility in TiO_2 (*118*).

The pump energy and temperature dependence combined indicate that electric field induced second harmonic generation (EFISH) from a transient electric field, created when electrons transfer to TiO_2 (Fig 6.2), is responsible for ΔI^{SHG}, for which the decay is proportional to the mobility of the charge carrier which has transferred to Ti. Additionally, the increased lifetime of the ΔI^{SHG} with increasing pump energy is the result of "hot" electrons with additional energy injecting further into TiO_2, requiring more time to drift back to the interface for recombination. This evidence proves that the electron follows a "boomerang" model, ballistic transfer out away from the interface and drifting back, instead of diffusing into the bulk TiO_2 conduction band (Fig 6.4b) Using this information, it is possible to approximate the excess energy (E^{ex}) of the electron at the time of transfer, following (*119*).

6.3 Approximating Ballistic Electrons Excess Energy

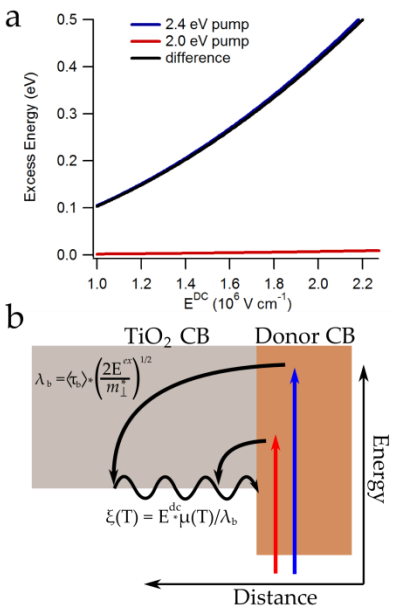

Figure 6.4: (a) Plot of excess energy vs interface electric field strength. (b) Simple schematic of ballistic hot electron injection and subsequent polaron drift from two different pump energies.

Because the electron hole are separated by only a few nanometers and the area excited by the pump pulse is on the order of a few hundred μm^2, the electric field generate by the separated charges can be modeled as a parallel plate capacitor, where

$$E^{DC} = \frac{1}{\varepsilon_r \varepsilon_0} \frac{2Q^{sep}}{A} \qquad (6.1)$$

where E^{DC} is the magnitude of the interfacial electric field, ε_r is the interface dielectric, ε_0 is the permittivity of free space, $2Q^{sep}$ is the total amount of separated charge (electron and hole), A is the irradiated area. The surface packing density of end-on aligned C132A QDs has been measured to densities as high as 2 nm^2 molecule^{-1} (*116*). The composite dielectric constant of the interface can be estimated as the average of the dielectric constant of the two materials. TiO_2 has a dielectric constant of $\varepsilon_r^{TiO_2} =$

86 (*120*), while the dielectric constant of graphene is much lower $\varepsilon_r{}^{\mathrm{C132}} = 2.5$ (*121*) giving a composite dielectric of $\varepsilon_r \approx 40$. Assuming 100% charge injection efficiency, $E^{DC} = 4.5\mathrm{x}10^6\ \mathrm{V\ cm^{-1}}$, which is 100 times greater than the interfacial field calculated for the PbSe QD system used by Tisdale et al., and more than enough to observe large EFISH responses in field effect transistors (*74*).

The overall path of the electron involves ballistic electron injection followed by hot electron relaxation to form band-edge polarons then Drude-like transport back to the interface under the influence of the interfacial electric field. The electrons cool to the conduction band edge through the emission of polar optical (LO) phonons (*122*). In TiO_2, these are high frequency phonon modes which vary little over the temperature range considered here (*123*). A ballistic electron traveling perpendicular to the c-axis in rutile with a given excess energy (E^{ex}) has a mean free path, λ_b, given by

$$\lambda_b = \langle \tau_b \rangle \cdot v_b = \langle \tau_b \rangle \cdot \left(\frac{2E^{ex}}{m_\perp^*}\right)^{1/2}. \qquad (6.2)$$

where $\langle \tau_b \rangle$ is the mean scattering time, v_b is the velocity of the ballistic electron, and $m_\perp^* = 1.2$ is the electron band mass in TiO_2 (*124*). The relaxed band-edge electrons (polarons) formed during the ballistic charge transfer will form a distribution of the form $n = n_0 \exp\left(-z/\lambda_b\right)$, where n is the local number concentration of polarons and z is the distance from the interface in the surface normal direction, with increasing z extending further into the bulk of the crystal. This distribution of polarons will then drift back to the interface where they are free to back transfer, reducing the overall amount of separated charges, according to,

$$Q^{sep} = Ae\int_{z=0}^{z=\infty} n(z,t)dz. \qquad (6.3)$$

Upon integration, it is shown that the decrease in separated charge over time is,

$$Q^{sep}(t) = Q_0 \exp\left(-\frac{v_p t}{\lambda_b}\right) \qquad (6.4)$$

where $v_p = \mu(T)E^{DC}$ is the polaron drift velocity and $\mu(T)$ is the polaron mobility at a given temperature.

The data has been fit to the form,

$$\Delta I^{(2\omega)}(t) = I_0^{(2\omega)} + \Delta I_0^{(2\omega)}\exp(-\xi t). \qquad (6.5)$$

Since $\Delta I^{(2\omega)}(t) \propto Q^{sep}(t)$ the pump-induced SH decay rate, ξ, is given by the expression $\xi(T) = E^{DC}\mu(T)/\lambda_b$. By combining this relationship with equation 6.2 we can get the following expression for excess energy

$$E^{ex} = \frac{\left(\frac{E^{DC}\mu(T)}{\langle\tau_b\rangle\xi(T)}\right)^2 m_\perp^*}{2}. \qquad (6.6)$$

Using eq. (6.6) and a typical polaron scattering rate of 50 fs, we can plot the excess energy as a plot of the electric field strength averaged for each temperature for the two pump energies (Fig. 6.3a). Assuming the additional energy of the 2.4 eV pump is shared equally between the electron and hole, if the electron transfer occurs prior to any relaxation, the additional excess energy is 0.2 eV, which when compared to the curve $E^{ex\,2.4\,eV}$-$E^{ex\,2.0\,eV} = E^{ex\,difference}$, corresponds to an $E^{DC} = 1.4x10^6 Vcm^{-1}$. As previously stated, the maximum E^{DC} of the system is $4.5\text{x}10^6$ V cm^{-1}. Correcting for

the excitation density ($\eta = 0.5$), the maximum expected $E^{DC} = 2.25X10^{6}V^{-1}cm^{-1}$, which is in relative agreement with the model.

The change in SH decay rates are 40 times faster for C132A QDs than for 5.7 nm PbSe QDs, although they both have $E^{ex} = 0.2\ eV$ (*24*). The modeling shows that this difference can be attributed to the increased packing density and low dielectric screening of the C132A QD.

References

1. "BP Statistical Review of World Energy," (June 2009).
2. S. E. Shaheen, D. S. Ginley, G. E. Jabbour, *MRS Bull* **30**, 10 (2005).
3. M. A. Green, *Progress in Photovoltaics,* **9**, 123 (2001).
4. M. A. Green, *Third Generation Photovoltaics* (Springer, Berlin, 2003), pp. 160.
5. M. Planck, *The Theory of Heat Radiation* (Dover, New York, 1959).
6. W. Shockley, H. J. Queisser, *J. Appl. Phys*. **32**, 510 (1961).
7. B. O'Regan, M. Gratzel, *Nature* **353**, 737 (1991).
8. B. A. Gregg, M. C. Hanna, *J. Appl. Phys*. **93**, 3605 (2003).
9. K. S. Leschkies et al., *Nano Letters*, **7**, 1793 (2007).
10. I. Robel, V. Subramanian, M. Kuno, P. V. Kamat, *J. Am. Chem. Soc*., **128**, 2385 (2006).
11. I. Gur, N. A. Fromer, M. L. Geier, A. P. Alivisatos, *Science*, **310**, 462 (2005).
12. E. J. D. Klem, D. D. MacNeil, P. W. Cyr, L. Levina, E. H. Sargent, *Appl. Phys. Lett.* **90**, 183113 (2007).
13. N. S. Sariciftci et al., *Appl. Phys. Lett*. **62**, 585 (1993).
14. G. Yu, J. Gao, J. C. Hummelen, F. Wudl, A. J. Heeger, *Science* **270**, 1789 (1995).
15. G. Li et al., *Nature Materials* **4**, 864 (2005).
16. W. U. Huynh, J. J. Dittmer, A. P. Alivisatos, *Science* **295**, 2425 (2002).
17. D. C. Olson, J. Piris, R. T. Collins, S. E. Shaheen, D. S. Ginley, *Thin Solid Films* **496**, 26 (2006).
18. R. D. Schaller, V. I. Klimov, *Phys. Rev. Lett.* **92**, 186601 (2004).
19. R. J. Ellingson et al., *Nano Letters* **5**, 865 (2005).
20. G. Nair, M. G. Bawendi, *Physical Review B* **76**, 081304 (2007).

21. J. J. H. Pijpers et al., *Nature Physics* **5**, 811 (2009).

22. R. T. Ross, A. J. Nozik, *J. Appl. Phys.* **53**, 3813 (1982).

23. Yan, X. Cui, B. Li, L-S., *Nano Lett.*, **10**, 1869-1873 (2010).

24. Tisdale et al. *Science,* **328**, 1543 (2010)

25. Ashcroft, N. W.; Mermin, N. D. *Solid State Physics*. Orlando, FL: W.B. Saunders

26. Efros, Al. L.; Efros A.L. *Sov. Phys.Semicond*. 1983, 16, 772.

27. L. E. Brus, *J. Chem. Phys.*,**80**, 4403 (1984).

28. N. Zettili, *Quantum Mechanics: Concepts and Applications* (Wiley, Chichester, 2001).

29. D. J. Norris, in Semiconductor and Metal Nanocrystals: Synthesis and electronic and optical properties, V. I. Klimov, Ed. (Marcel Dekker, New York, 2004), chap. 2.

30. C. B. Murray, C. R. Kagan, M. G. Bawendi, *J. Am. Chem. Soc.*, **120**, 5343 (1993).

31. C. B. Murray, C. R. Kagan, M. G. Bawendi, *Annu. Rev. Mater. Sci.*, **30**, 545 (2000).

32. C. A. Leatherdale, M. G. Bawendi, *Physical Review B*, **63**, 165315 (2001).

33. Li, L.-S.; Yan, X. *J. Phys. Chem. Lett.*, **1**, 2572- 2576 (2010).

34. Yan, X.; Cui, X.; Li, L.-S. *J. Am. Chem. Soc.*, **132**, 5944-5945 (2010).

35. R. R. Nair et al., *Science*, **320**, 1308–1308 (2008).

36. Mueller, M. L.; Yan, X.; Dragnea, B.; Li, L.-S. *Nano Lett.*, **11**, 56–60, (2011).

37. A. Pandey, P. Guyot-Sionnest, *Science*, **322**, 929-932 (2008).

38. Klimov, V. *J. Phys. Chem. B*, **104**, 6112–6123 (2000).

39. Klimov, V.; McBranch, D. W. *Phys. Rev. Lett.*, **80**, 4028–4031 (1998).

40. Efros, A. L.; Kharchenko, V. A.; Rosen, M. *Solid State Commun.*, **93**, 281–284 (1995).

41. Wang, L.-W.; Califano, M.; Zunger, A.; Franceschetti, A. *Phys. Rev. Lett*., **91**, 056404 (2003).

42. Cooney, R. R.; Sewall, S. L.; Anderson, K. E. H.; Dias, E. A.;Kambhampati, P. *Phys. Rev. Lett.,* **98**, 177403 (2007).

43. Cooney, R. R.; Sewall, S. L.; Dias, E. A.; Sagar, D. M.; Anderson, K. E. H.; Kambhampati, P. *Phys. Rev. B* 2007, **75**, 245311.

44. Schroeter, D. F.; Griffiths, D. J.; Sercel, P. C. *Phys. Rev. B*, **54**, 1486–1489 (1996).

45. Sercel, P. C. *Phys. Rev. B*, **51**, 14532–14541 (1995).

46. Guyot-Sionnest, P.; Wehrenberg, B.; Yu, D. *J. Chem. Phys*., **123**, No. 074709 (2005).

47. D. M. Adams et al., *J Phys Chem B*, **107**, 6668 (2003).

48. A. Nitzan, Chemical dynamics in condensed phases: relaxation, transfer and reactions in condensed molecular systems (Oxford University Press, Oxford ; New York, 2006), pp. 719.].

49. R. A. Marcus, N. Sutin, *Biochim. Biophys. Acta* **811**, 265 (1985).

50. D. M. Newns, *Phy. Rev.* **178**, 1123 (1969).

51. P. Liljeroth, *Phys. Rev. Lett.,* **97**, 096803 (2006).

52. X. Y. Zhu, *Surface Science Reports* **56**, 1 (2004).

53. N. A. Anderson, T. Q. Lian, *Annu. Rev. Phys. Chem.* **56**, 491 (2005).

54. D. F. Watson, G. J. Meyer, Annu. *Rev. Phys. Chem*. **56**, 119 (2005).

55. P. R. Yu et al., *J Phys Chem B* **110**, 25451 (2006).

56. P. V. Kamat, *J. Phys. Chem. C* **111**, 2834 (2007)

57. S. Jin, A. Martinson, G. Wiederrecht, *J. Phys. Chem C*, **116**, 2097-3104 (2012).

58. J. L. Blackburn, D. C. Selmarten, A. J. Nozik, *J Phys Chem B* **107**, 14154 (2003).

59 J. L. Blackburn et al., *J Phys Chem B* **109**, 2625 (2005).

60. B. R. Hyun, Y. W. Zhong, A. C. Bartnik, L. F. Sun, H. D. Abruna, F. W. Wise, J. D. Goodreau, J. R. Matthews, T. M. Leslie, N. F. Borrelli, *ACS Nano* **2**, 2206 (2008).

61. S. Y. Jin, T. Q. Lian, *Nano Letters* **9**, 2448-2458 (2009).

62. C. Burda, S. Link, M. Mohamed, M. El-Sayed, *J Phys Chem B* **105**, 12286 (2001).

63. B. C. Fitzmorris, G. K. Larsen, D. A. Wheeler, Y. Zhao, J. Z. Zhang, *J. Phys. Chem. C*, **116**, 5033-5041 (2012).

64. E. Canovas et al., *Nano Lett.*, **11**, 5234-5239 (2012).

65. D. J. Griffiths, *Intro. to Electrodynamics 3rd ed.*, Prentice Hall, Upper Saddler River, c. 1999.

66. R. W. Boyd, *Nonlinear Optics 2nd ed.*,Academic Press, Boston,c. 2000, p. 439.

67. A. Yariv, *Quantum Electronics* (Wiley, New York, 1989).

68. M. C. Downer, B. S. Mendoza, V. I. Gavrilenko, *Surf Interface Anal* **31**, 966 (2001).

69. B. Dick, A. Gierulski, G. Marowsky, G. A. Reider, *Applied Physics B-Photophysics and Laser Chemistry* **38**, 107 (1985).

70. E. Kobayashi, G. Mizutani, S. Ushioda, *Japanese Journal of Applied Physics Part 1-Regular Papers Short Notes & Review Papers* **36**, 7250 (1997).

71. M. Omote et al., *Journal of Physics-Condensed Matter*, **17**, S175 (2005).

72. H. Lee, R. K. Chang, N. Bloembergen, *Phys. Rev. Lett.* **18**, 167 (1967).

73. T. F. Heinz, in *Nonlinear Suface Electromagnetic Phenomena*, H. Ponath, G. I. Stegeman, Eds. (Elsevier, Amsterdam, 1991), pp. 353-416.

74. O. A. Aktsipetrov *et al.*, *Phys. Rev. B* **60**, 8924 (1999).

75. P. Guyot-Sionnest, W. Chen, Y. R. Shen, *Phys. Rev. B* **33**, 8254 (1986).

76. A. Nahata, T. F. Heinz, *Opt. Lett.* **23**, 67 (1998).

77. C. B. Murray, C. R. Kagan, M. G. Bawendi, *Science*, **270**, 1335–1338 (1995).

78. E. V. Shevchenko et al. Nature, 439, 55–59 (2006).

79. D. S. Ginger, N. C. Greenham, J. Appl. Phys., 87, 1361–1368 (2000).

80. C. A. Leatherdale et al. Phys. Rev. B, 62, 2669–2680 (2000).

81. N. Y. Morgan et al. Phys. Rev. B, 66, 075339 (2002).

82. M. Drndic´ et al. J. Appl. Phys., 92, 7498–7503 (2002).

83. A. J. Houtepen, D. Kockmann, D. Vanmaekelbergh, *Nano Lett.,* **8**, 3516–3520 (2008).

84. T. S. Mentzel et al., *Phys. Rev. B*, **77**, 075316 (2008).

85. M. V. Artemyev et al., *J. Phys. Chem. B*, **104**, 11617-11621 (2000).

86. D. I. Kim, *J. Phys. Chem. B*, **107**, 6318-6323 (2003).

87. J. H. Warner, *Adv. Mater.,* **20**, 784-787 (2008).

88. I. U. Arachchige, S. L. Brock, *J. Am. Chem. Soc.*, **128**, 7964-7971 (2006).

89. D. Yu, C. Wang, P. Guyot-Sionnest, S*cience*, **300**, 1277-1280 (2003).

90. D. V. Talapin, C. B. Murray, *Science*, **310**, 86-89 (2005).

91. M. Law et al., *J. Am. Chem. Soc.*, **130**, 5974-5985 (2008).

92. J. M. Luther et al. *ACS Nano*, **2**, 271-280 (2008).

93. J. E. Murphy, M. C. Beard, A. J. Nozik, *J Phys Chem B*, **110**, 25455 (2006).

94. Y. F. Lu, D. J. Choi, J. Nelson, O. B. Yang, B. A. Parkinson, *J. Electrochem. Soc.*, **153**, E131 (2006).

95. Q. Q. Dai et al., *Acs Nano,* **3**, 1518 (2009).

96. Wise, F. W. *Acc. Chem. Res*, **33**, 773–780. (2000)

97. P. M. Echenique, J. B. Pendry, *J. Phys. C*: *Solid State Phys.*, **11**, 2065-2075 (1978).

98. Cragg, G. E.; A. L. Efros, *Nano Lett*., **10**, 313 – 317. (2010)

99. O. Millo, D. Katz, Y. W. Cao, U. Banin, *Phys. Rev. Lett.*, **86**, 5751 – 5754 (2001)

100. Nozik, A. J. Quantum Dot Solar Cells. *Physica E* **2002**, *14*, 115-120

101. Le´vy-Cle´ment, C.; Tena-Zaera, R.; Ryan, M. A.; Katty, A.; Hodes, G. . *Adv. Mater*. **2005**, *17*, 1512-1515

102. Pernik, D. R.; Tvrdy, K.; Radich, J. G.; Kamat, P. V. *J. Phys. Chem. C* **2011**, *115*, 13511-13519

103. Kaake, L.; Jailaubekov, A.; Williams, K.; X.-Y. Zhu. *Appl. Phys. Lett.* **2011**, *99*, 083307-083309

104. Reiss, P.; Bleuse, J.; Pron,. *Nano Lett.* **2002**, *2*, 781-784

105. Yu, W. W.; Qu, L.; Guo, W.; Peng, X. *Chem. Mater.* **2004**, *16*, 560-560

106. Chi, C-F.; Cho, H-W.; Teng, H.; Chuang, C-Y.; Chang, Y-M.; Hsu, Y-J.; Leem Y-L. *Appl. Phys. Lett.* **2011**, *98*, 0121011-0121013

107. Markus, T. Z.; Itzhakov, S.; Alkotzer, Y. I.; Cahen, D.; Hodes, G.; Oron, D.; Naaman, R. *J. Phys. Chem. C* **2011**, *115*, 13236-13241

108. Lu, Y.; Jaeckel, B.; Parkinson, B. *Langmuir* **2006**, *22*, 4472-4475

109. R. D. Schaller, J. M. Pietryga, S. V. Goupalov, M. A. Petruska, S. A. Ivanov, V. I. Klimov, *Phys. Rev. Lett.* **95**, 196401 (2005).

110. J. B. Asbury, N. A. Anderson, E. Hao, X. Ai, T. Lian, *J. Phys. Chem. B*, , **107**, 737 (2003**).**

111. Kambhampati, P. *J. Phys. Chem. C* **2011**, 115, 22089-22109

112. Mora-Seró, I.; Bisquert, J. *Nano Lett.* **2003**, *3*, 945-949

113. Bisquert, J.; Zaban, A.; Salvador, P. *J. Phys. Chem. B.* **2002**, *106*, 8774-8782

114. Nozik, A. J. *Nano Lett.*, **10**, 2735- 2741 (2010).

115. X. Yan, et al. *J. Phys. Chem. Lett.*, **2**, 1119-1124 (2011).

116. I. P. Hamilton, B. Li, X. Yan, L-S. Li, *Nano Lett.*, **11**, 1524-1529 (2011).

117. K. D. Dobsen, A. J. McQuillan, *Spectrochimica Acta A*, **55**, 1395-1405 (1998)].

118. E. Hendry, F. Wang, J. Shan, T. F. Heinz, M. Bonn, *Physical Review B* **69** (2004).

119. W. A. Tisdale, dissertation, University of Minnesota, 2010 (0130E_11263)

120. V. V. Meriakri, E. F. Ushatkin, *Instrum. Exp. Tech*. **16**, 143 (1973).

121. V. S. Morozov, K.S. Novoselov, A.K. Geim, *Physics-Uspekhi* **51**, 744-748, (2008).

122. K. F. Brennan, *The Physics of Semiconductors*, Cambridge University Press, (1999).

123. J. F. Baumard, F. Gervais, *Physical Review B* **15**, 2316 (1977).

124. K. M. Glassford, J. R. Chelikowsky, *Physical Review B* **46**, 1284 (1992).